

Landslides (2020) 17:755–776  
 DOI 10.1007/s10346-019-01316-2  
 Received: 19 March 2019  
 Accepted: 5 November 2019  
 Published online: 2 December 2019  
 © Springer-Verlag GmbH Germany  
 part of Springer Nature 2019

Emma Cody · Daniel Draebing · Samuel McColl · Simon Cook · Marc-Andre Brideau

## Geomorphology and geological controls of an active paraglacial rockslide in the New Zealand Southern Alps

**Abstract** Geological structures precondition hillslope stability as well as the processes and landslide mechanisms which develop in response to deglaciation. In areas experiencing glacier retreat and debuttressing, identifying landslide preconditions is fundamental for anticipating landslide development. Herein, the ~ 150 M m<sup>3</sup> Mueller Rockslide in Aoraki/Mount Cook National Park, New Zealand, is described; and we document how preconditions have controlled its morphology and development in response to thinning of the adjacent Mueller Glacier. A combination of geomorphological and geotechnical mapping—based on field, geophysical and remote sensing data—was used to characterise the rock mass and morphology of the rockslide and surrounding hillslope. Mueller Rockslide is identified as a rock compound slide, undergoing dominantly translational failure on a dip slope. The crown of the rockslide is bounded by several discontinuous, stepped scarps whose orientation is controlled by joint sets; these scarps form a zone of toppling that is delivering rock debris to the main rockslide body. Surface and subsurface discontinuity mapping above the crown identified numerous joints, fractures and several scarps that may facilitate continued retrogressive enlargement of the rockslide. The presence of lateral release structures, debuttressing of the rockslide toe and steeply dipping bedding suggest that the rockslide may be capable of evolving to a rapid failure.

**Keywords** Paraglacial · Rockslide · Landslide preconditions · UAV · Natural hazard

### Introduction

Topographic, environmental and geological conditions predispose alpine landscapes to hillslope instability (McColl and Draebing 2019). Consequently, mass movements are a significant process shaping alpine and mountainous areas as well as a significant natural hazard. While slope failure can occur in a variety of ways in mountainous terrain, large deep-seated slope failures such as deep-seated gravitational slope deformations (DSGSD) and rockslides are primary hillslope modification processes and their evolution remains a subject of scientific enquiry.

DSGSD predominantly occur in steep relief and are commonly expressed as large interconnected networks of fractures and tension cracks as well as with toe bulging, uphill and downhill facing scarps and significantly displaced geomorphic features (Beck 1968; Dramis and Sorriso-Valvo, 1994; Bovis and Evans, 1996; Agliardi et al., 2001; Agliardi et al. 2009a). DSGSD deform slowly over centuries to millennia (El Bedoui et al. 2009; Agliardi et al. 2009b; Pánek et al. 2011b; Pánek and Klimeš 2016); however, they have the potential to accelerate and fail catastrophically as large rockslides or rock avalanches (Pánek et al. 2009; Kilburn and

Petley 2003; Gori et al. 2014). Rockslides, whether preceded or not by DSGSD activity, can reach similar sizes to DSGSD (> 100 Mm<sup>3</sup>) but differ in that they more commonly move via sliding along one or more discrete failure surfaces, rather than through internal deformation and toe bulging (Hungri et al. 2014). Upward facing scarps are less characteristic of rockslides, and they tend to involve more intact rock mass blocks in comparison with DSGSD (Crosta and Agliardi 2003; Crosta et al. 2014). As with DSGSD, they can fail progressively, evolving towards rapid failure, but may involve different failure processes.

Given the potentially large size (> 100 Mm<sup>3</sup>) of DSGSDs and rockslides and their ability to generate long-runout, rock avalanches, these slope failures are considered to be a major natural hazard in alpine landscapes. Although they have long been recognised within the scientific community (Nemcok et al. 1972; Mahr 1977; Radbruch-Hall 1978; Bovis 1982; Crosta et al. 2013; Chigira and Kihō 1994), there is still much to understand of the processes driving their evolution towards failure. As these large rock slope failures often develop over centuries to millennia, as well as occurring in steep and difficult terrain, understanding internal factors influencing development is critical for assessing the failure potential of the landslide.

Worldwide, many large DSGSD and rockslides have been recognised in oversteepened glacial valleys (Agliardi et al. 2009b; McColl and Davies 2013; Barbarano et al. 2015; Coquin et al. 2015). In alpine landscapes, glacier debuttressing—where ice support is removed from the toe of a hillslope—is considered a primary influence on preparing DSGSD or rockslide formation (Ballantyne 2002). However, rainfall and changes in groundwater (Pánek et al. 2011a; Nishii et al. 2013), earthquakes (Crozier et al. 1995; Aringoli et al. 2016), gravitational or topographic stresses (Martinotti et al. 2011) and river incision (Hou et al. 2014) have all been attributed with triggering hillslope failures in both glaciated and non-glaciated terrain. Given that large rock slope failures occur in a variety of rock types and rock masses, climate conditions and tectonic settings, identifying a common control or main trigger is difficult. As it stands, DSGSD and rockslides appear to commonly form along pre-existing or reactivated tectonic structures (faults, fractures and joints) (Agliardi et al. 2001; Ghirotti et al. 2011; Ambrosi and Crosta 2011; Jaboyedoff et al. 2013) which constrain their size and morphology. Geological structures and steep relief precondition instabilities and are key for understanding how preparatory factors like debuttressing, fluvial incision and strength degradation allow slopes to evolve to failure.

Investigations into DSGSD and rockslides in glaciated valleys have primarily focused on those which formed or failed following prehistoric (pre Little Ice Age; LIA) glacier retreat (Cossart et al. 2008; Hewitt et al. 2008; Ballantyne and Stone, 2013; Ballantyne

et al. 2014a; Ballantyne et al. 2014b; Ballantyne and Stone 2009) as a result of debuttressing and loss of support to the slope. More recently, effort has been directed towards monitoring the response of hillslopes currently undergoing deformation following glacier retreat (Clayton et al. 2017; Fey et al. 2017; Kos et al., 2016; Glueer et al. 2019). For example, an acceleration of landslide movement and a change in movement mechanisms have been observed to coincide with glacier retreat and debuttressing at the Moosfluh Landslide beside the Aletsch Glacier in Switzerland (Kos et al., 2016; Glueer et al. 2019) and at the Marzell Rockslide in Austria (Fey et al. 2017).

While monitoring studies have highlighted how some slopes are currently accelerating in response to recent glacier retreat, deformation may have been occurring within the rock slope for centuries to millennia (Eberhardt et al. 2004; Brideau et al. 2009; Ballantyne et al. 2014a; Riva et al., 2018). Progressive failure (i.e. the progressive loss of strength of a rock mass) within paraglacial rock slopes occurs through stress changes induced by glacial erosion, ice load fluctuations, in situ stress modification and thermal and hydro-mechanical processes (McColl 2012a; Jaboyedoff et al. 2013; Grämiger et al. 2017; Grämiger et al. 2018). While a rock slope may currently be undergoing rapid deformation, it is likely that strength degradation has been ongoing through several repeated cycles of glacier advance and retreat. Further, as glaciated slopes begin to develop instability, their movement might involve deformation of its buttressing glacier (McColl and Davies 2013), creating a complex interaction between the glacier and the mass movement. Such interactions are likely to affect whether a slope catastrophically collapses, the timing of collapse and how the mass movement affects glacier and sediment transport dynamics.

In this study, we investigate the geomorphology and structural features of an active deep-seated slope failure, the Mueller Rockslide, whose development coincides with thinning of an adjacent glacier. Mueller Rockslide was described by McColl and Davies (2013) as an example of a large (~ 150 Mm<sup>3</sup>) deep-seated gravitational slope deformation, undergoing gradual deformation adjacent to a retreating glacier. The study combines geomorphological mapping with geotechnical, geophysical, and remote sensing techniques to identify discontinuity sets and other structures in and around the rockslide. The structures are interpreted within the context of the geomorphological and geological setting of the rockslide. We explore how these structures have preconditioned failure of this slope and identify the potential for retrogressive enlargement and catastrophic development of the rockslide. Our research contributes to the understanding of how geological structures precondition paraglacial rock slope failures and influence their response to contemporary glacier retreat.

### Study area

Mueller Rockslide is in Aoraki/Mount Cook National Park, New Zealand (Fig. 1), situated on the western flank of the Sealy Range. The rockslide was first identified by Hancox (1994), as part of a study on the stability of an alpine mountain hut. At that time, the hut (referenced as Old Hut herein) was situated on the eastern edge of the Sealy Range, which was experiencing localised subsidence in a large slump block. Due to safety concerns, the hut was removed and rebuilt 500 m south-west along the range in 2003. During the investigation, Hancox (1994) identified and described a

much large slope failure (herein the Mueller Rockslide), affecting the western side of the Sealy Range, which Hancox described as a large block slide with an extensive headscarp area and a large rift-zone/graben. The hut is now about 200 m east of a series of large (10–20 m high, 30–50 m long) scarps that appear to define the head scarp of the rockslide (Hancox 1998). Above the rockslide, in the vicinity of the newly located Mueller Hut, several large fractures have been monitored since 1994 with opening detected of between 6 and 66 mm (Archibald et al. 2016). Annual GPS measurements of survey pins about 700 m west of Mueller Hut within the rockslide indicate movement rates of 1 m per year between 2010 and 2012 (McColl 2012b).

The shape and stability of the Sealy Range reflects its history of tectonic and glacial processes. The range is about 25 km east of the boundary between the Pacific and Australian tectonic plates, which for the past 5 million years has been expressed by the Alpine Fault. Regional shortening and compression have resulted in faulting, folding and fracturing of the Torlesse Group greywacke sandstones and argillite and semischist (low-grade schist of textural zone IA, IIB) which make up the Sealy Range (Cox and Barrell 2007). The Mueller Rockslide is located on the western side of the Sealy Range, on the western limb of the tightly folded north-plunging Kitchener anticline (Lillie and Gunn 1964), which formed initially from east-west compression (Fig. 2). Within and near the rockslide body, bedding dips westward at roughly 30–60°, with the Mueller Rockslide forming within the dip slope of the interbedded greywacke (Lillie and Gunn 1964; McColl and Davies 2013) although most of this is heavily mantled with debris material. Currently, the Mueller Rockslide abuts onto the margin of the Mueller Glacier, which is undergoing rapid thinning and terminus retreat. The Mueller Glacier has retreated by over 1 km (Gellatly 1985; Kirkbride and Warren 1999) since the Little Ice Age (LIA) ~ 200–250 years ago (Fig. 1), but it is still approximately 3.5 km down-valley from the Mueller Rockslide (Winkler 2018). Glacier debuttressing has occurred through thinning of the glacier and has been in the order of some 100 m since the LIA, as inferred here from abandoned lateral moraine ridges on the slopes near the rockslide as well as documented at the terminus (Gellatly 1985; Kirkbride and Warren 1999). The remaining thickness of the glacier at the toe of the Mueller Rockslide is unknown, but based on valley cross section extrapolation, it is estimated to be < 100 m thick at the southern (upper valley) end of the rockslide. The glacier at the northern end may have melted completely, becoming disconnected from the down valley end of the glacier (Fig. 2).

### Methods

#### Topographic data and aerial photography

High-resolution topographic data and an orthophoto mosaic were obtained using structure-from-motion (SfM) photogrammetry (Fig. 3) for mapping the rockslide and surrounding slopes. Photos were collected in February 2017 from a DJI Phantom 3 Professional unmanned aerial vehicle (UAV). Photos were captured from an above ground altitude of 60–120 m, in both oblique (30° from nadir) and nadir camera orientations to achieve a minimum of 75% forward and 60% side photo overlap. The SfM software Agisoft Photoscan was used to produce a dense point cloud that was decimated to a 0.25-m resolution DEM, and a 5-cm pixel-resolution orthomosaic image. The georeferencing of the SfM

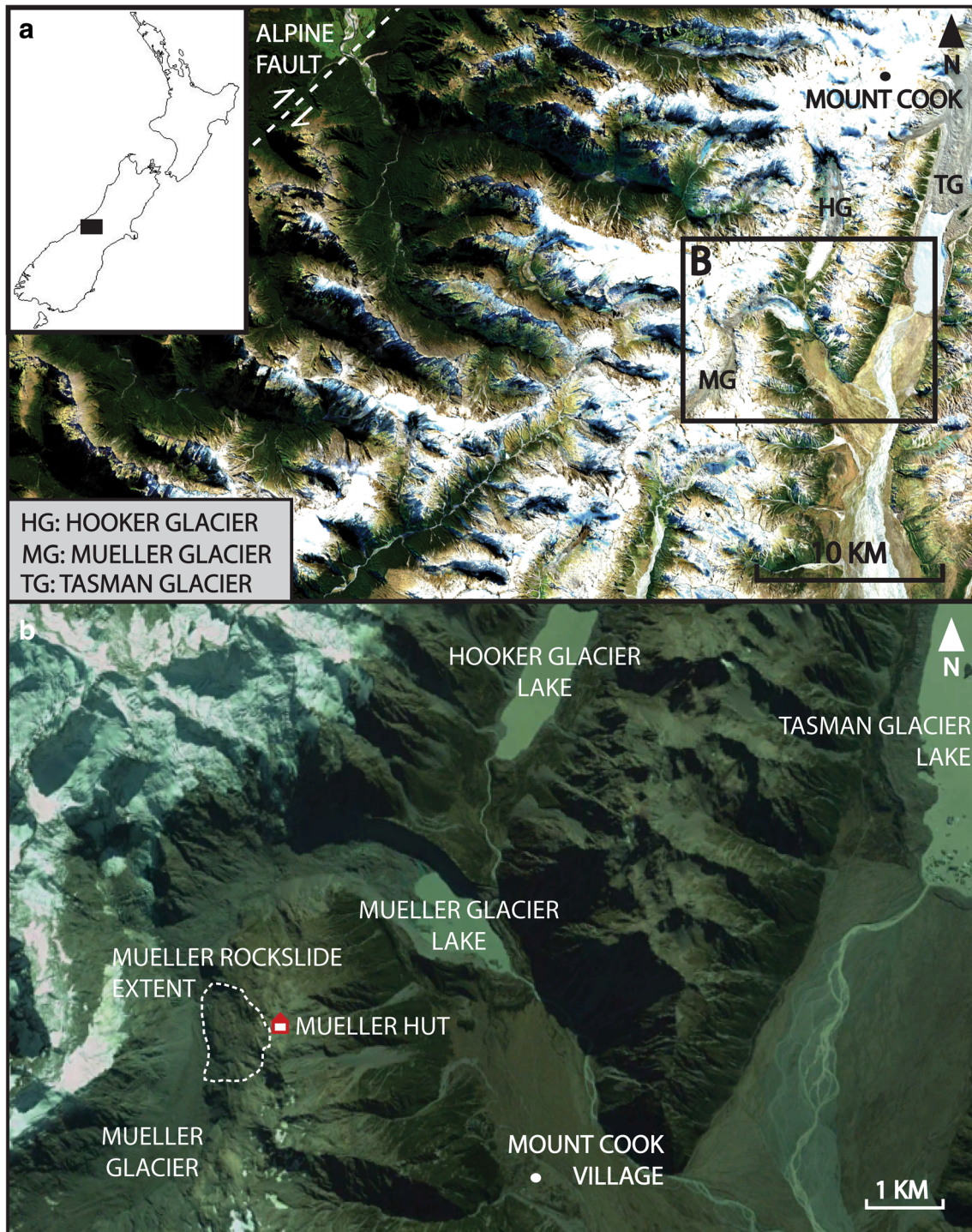


**Fig. 1** (A) Location map of Mount Cook and surrounding area. (B) Mount Cook Village and surrounding area. Mueller Rockslide estimated boundary is represented by the dashed white line with Mueller Hut sitting to the east

model was provided by 22 ground control point (GCP) targets surveyed with a Trimble R10 GPS, with a 5-km RTK baseline correction, and referenced against the national survey network (using B8Y2 UNWIN geodetic benchmark, and the New Zealand Geodetic Datum 2000 and New Zealand Vertical Datum 2016). The GCPs were distributed asymmetrically, due to difficulty deploying them in steep, fractured terrain along the glacier and lower and

southern slopes of the rockslide (Fig. 3). The Photoscan estimate of GCP vertical uncertainty was an RMSE 0.156 m. We provided an independent assessment of this modelled error by comparing the modelled DEM elevations with our own 10 independent spot height elevations measured with RTK GPS. The mean difference and RMSE we calculated were 0.35 m and 0.59 m respectively, with a maximum of 1.75 m (Table 1). These vertical error values are

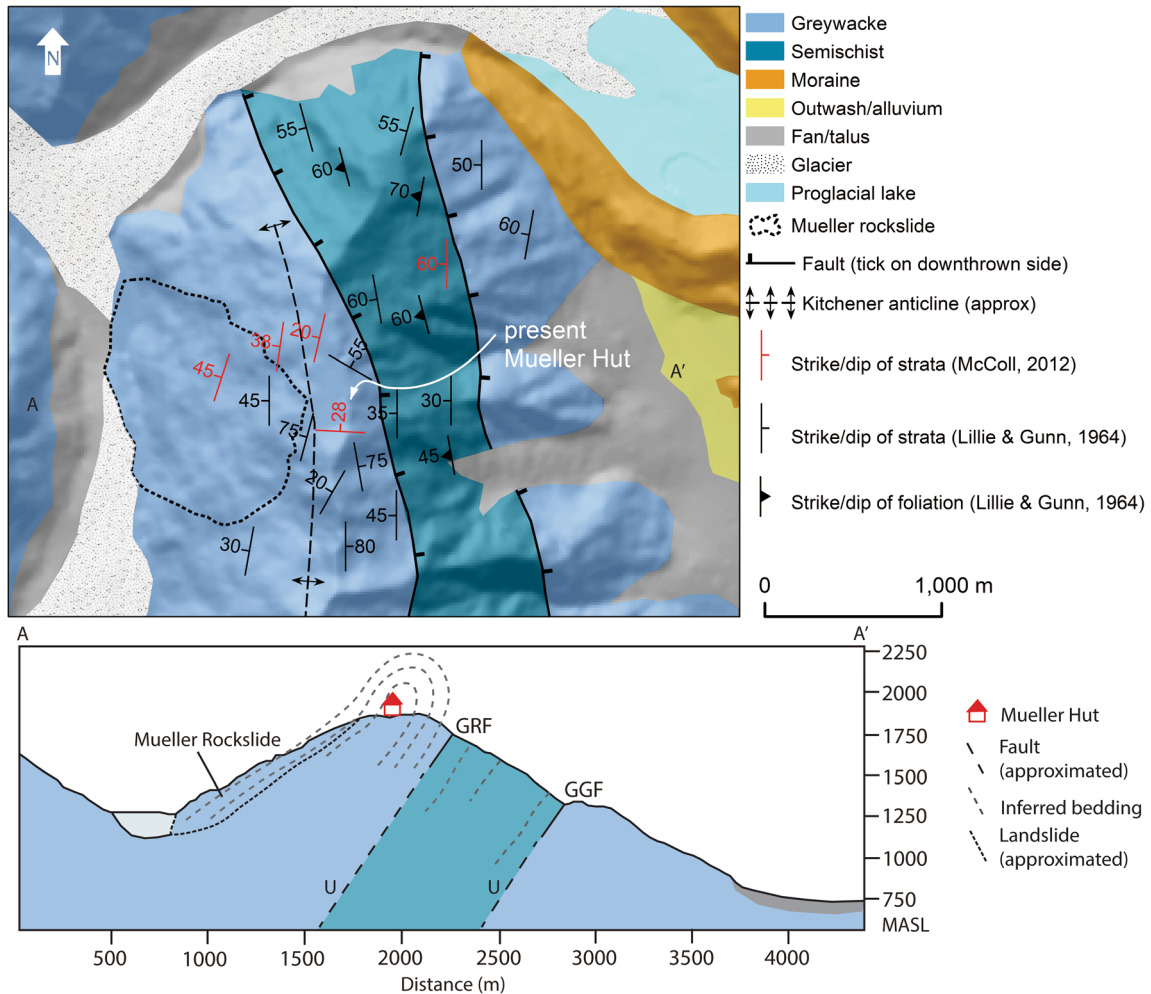


**Fig. 2** Geological map of Sealy Range and cross-sectional profile of the Kitchener Anticline (informed by mapping by Lillie and Gunn 1964 and McColl 2012a). Glacier extent and Mueller Rockslide outline are as mapped in this study, based on aerial imagery from 2010–2017. GRF and GGF highlight the Green Rock Fault and Great Groove Fault

mostly representative of the area inside our GCP distribution; therefore, we have lower confidence in the model accuracy in the western and southern parts of the model outside of the GCP distribution. However, the combination of oblique and nadir convergent photographs will have reduced the amount of radial distortion in the model periphery, as shown by James and Robson (2014), and where GCPs were not available, the aircraft's built-in GPS (better than 10 m accuracy) provided camera positions for lens optimisation. We consider the resulting accuracy of the DEM to be adequate for the purposes intended here: to support geomorphological and geotechnical mapping of the rockslide and surrounding slopes.

### Geomorphological and fracture mapping

A combination of field observations and remote-sensing was used to map the geomorphology and structures present at the site. Using the SfM hillshade model and orthomosaic, landforms and features on and around the rockslide were mapped, including scarps, major fractures, lateral moraines, and areas of debris cover and bedrock outcrop. Detailed field mapping over three

consecutive summers was completed in 2017, 2018 and 2019. Features mapped in the field included scarps, fractures, tension cracks and bedding. A total of 41 bedding measurements and 206 joint measurements (including fractures and tension cracks) were taken in the field.

Mapping of discontinuity locations and orientations was done in the field at accessible bedrock outcrops on the rockslide and ridge, and along the geophysical transects (described below). Discontinuities were also measured along one to two scan-line surveys perpendicular to each geophysics transect (Fig. 3). For less accessible locations of the site, major fractures were mapped remotely using Point Cloud Viz (Mirage Technologies SL) to select fractures in 3D space using each fracture face. Discontinuities were plotted on stereonet, with pole-to-plane density contours, using the software DIPS (Rocscience, 2017), to identify orientation patterns and major fracture sets within the fracture network. Discontinuities were grouped into two structural domains: Domain 1 within the rockslide including the rockslide body and headscarp and Domain 2 outside the rockslide and along the ridgeline. Kinematic analysis was conducted for both structural domains

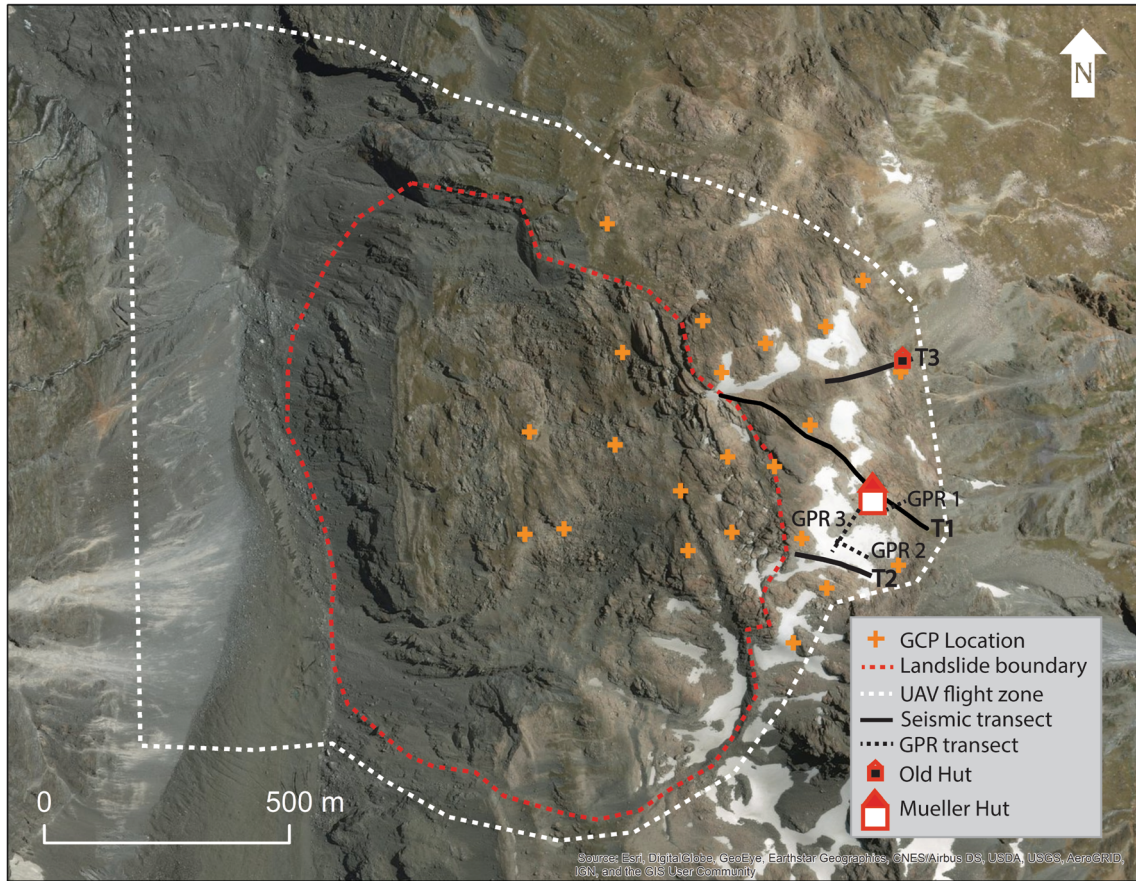


**Fig. 3** Approximate rockslide outline, extent of the UAV flights for photogrammetry and ground control points (GCPs), spot height survey marks used in Table 1, and the geophysics transects. Imagery is 0.75 m LINZ aerial photo (~ 2004–2010)

for plane, wedge and flexural toppling failure, with the aim of evaluating the feasibility of simple structurally controlled failure mechanisms (following Kliche 1999). Average slope dip and dip direction obtained from the SfM-derived digital surface model

were used in the kinematic analysis. A friction angle of  $33^\circ$  was taken from previous tilt test results (McCull 2012b) assuming failure along an argillite bedding surface. Argillite and siltstone beds are a common feature of the greywacke within the study area

**Table 1** Comparison between selected spot heights and equivalent DEM elevations. Distance to nearest GCP indicates model performance away from model control points

Spot height ID	Spot height elevation (m) (NZVD2016)	DEM elevation (m) (NZVD2016)	Elevation difference (m)	Distance to nearest GCP (m)
1	1844.62	1844.69	0.07	16.3
2	1779.28	1779.09	0.19	14.9
3	1472.66	1472.21	0.45	11.1
4	1686.85	1686.55	0.29	54.6
5	1714.83	1714.78	0.05	17.9
6	1787.33	1787.39	0.06	11.5
7	1786.96	1786.70	0.26	37.7
8	1812.91	1812.77	0.15	112.7
9	1815.55	1815.37	0.18	35.9
10	1554.84	1556.59	1.75	99.1
Mean			0.35	41.17

and their lower strength compared with sandstone makes them the most likely structural weakness along which bedding failure may be facilitated. This friction angle may be greater than that of a fully formed sliding surface (i.e. at residual strength) in argillite, so is treated as an upper estimate for the frictional strength of the argillite beds.

### Geophysical surveys

Seismic refraction tomography (SRT) and ground penetrating radar (GPR) were used to image the subsurface rock mass around the rockslide headscarp, Sealy Range Ridgeline and Mueller Hut. The steep and highly unstable topography of the landslide body made it impossible to conduct geophysical surveys along the rockslide. The geophysical surveys were used to identify rock mass discontinuities and better characterise the subsurface extent and nature of fractures, either identified or obscured by scree at the surface. In particular, the subsurface mapping was to help evaluate the potential for rockslide retrogression through identification of incipient shear surfaces east of the Mueller Rockslide crown. SRT has been previously used to investigate the internal structure of rock slope instabilities, such as the Åknes Rockslide in western Norway (Ganerød et al. 2008; Heincke et al. 2010), the slope instability at Randa in the Swiss Alps (Heincke et al. 2006), the La Séchilienne Rockslide in the French Pre-Alps (Meric et al. 2005) and several rockslides in Tien Shan, Kyrgyzstan (Havenith et al. 2000; Havenith et al. 2002). GPR has been used in previous rockslide and rock fall studies to investigate individual fractures and discontinuities (Toshioka et al. 1995; Theune et al. 2006) as well as stratigraphic analysis (Davis and Annan 1989). Here, we combine both methods to maximise the potential information produced regarding shallow (< 20 m) subsurface rock mass conditions.

Three combined geophysics transects using SRT and GPR were deployed along Sealy Ridgeline in a roughly east-west direction (T1–T3 in Fig. 3), targeting major fractures visible at the surface, and where possible, following accessible bedrock outcrop. In addition, 3 GPR transects were completed in the immediate area of Mueller Hut (Fig. 3). Transect 1 (Mueller Hut transect) extends from the eastern Sealy Range ridgeline, past the present-day Mueller Hut to the main rockslide headscarp. Transect 2 (Mount Ollivier transect) is located farthest to the south, stretched east-west along the northern slope of Mount Ollivier. Transect 3 (Old Hut transect) is nearer to the northern end of the rockslide and stretches from eastern Sealy Range ridgeline near the former Mueller Hut, west to the rockslide headscarp. SRT was completed using repeated overlapping transects of 24 geophones. Transect 1 had geophone spacing of 6 m and consisted of 4 overlapping transects (each 138 m long) resulting in a total length of 531 m. Transects 2 and 3 had a geophone spacing of 8 m with 3 additional offset shots after geophone 24 resulting in a total transect length of 204 m. Different geophone spacing resulted in different resolutions for the seismic tomographies which range from 1.5 m at T1 to 2 m at T2 and T3.

Seismic waves for the SRT survey were generated by sledgehammer shots between each geophone and three offset shots before or after the first and last geophone. Five shots were stacked to increase signal-to-noise-ratio. Geophone and offset shot positions were recorded using a Trimble R10 RTK DGPS and implemented in the data processing using Reflex W 7.0 (Sandmeier

2012). First arrivals were picked manually. Raw data analysis was performed using the approach by Krautblatter and Draebing (2014). The raw data were inverted using the SIRT algorithm of Reflex W and ray path tracing was performed to check ray coverage. The quality of the final tomographies was calculated and total absolute time difference (3.96–4.72 ms) and root mean square error (5.58–6.27 ms) are in an acceptable range of 1/4 of the seismic wave amplitudes at Mueller Rockslide (10 to 20 ms).

The volumetric fracture density ( $P_f$ ) for the rock mass was calculated using the equation by Clarke and Burbank (2011) and is expressed as a percentage:

$$P_f = \frac{V_f}{(V_r - V_f)} \left( \frac{V_r}{V_p} - 1 \right)$$

where  $V_p$  is the subsurface p-wave velocity measured by the seismic survey,  $V_r$  is the intact rock velocity, and ( $V_f$ ) is the velocity of the fracture material. Rock samples collected from the field were cut into 6.27 cm wide and 4.5 to 5.8 cm long cores and used to quantify  $V_r$  in the lab in parallel and perpendicular directions. A Geotron ultrasonic generator USG40 in combination with Geotron preamplifier VV51 and 350 kHz sensors generated the seismic signal. Seismic signals were recorded using a PICO oscilloscope and data analysed using the software Geotron Lighthouse UMPC. Intact rock p-wave velocity ( $V_r$ ) is  $0.54 \pm 0.4 \text{ km s}^{-1}$  and anisotropy on rock core scale according to Draebing and Krautblatter (2012) is 6 to 8%. We assumed that the fracture infill is air and, therefore,  $V_f$  is the velocity of air ( $0.33 \text{ km s}^{-1}$ ).

Ray path tracing was performed to estimate fracture location and persistence using the technique developed by Phillips et al. (2016). Ray density indicates the number of rays crossing a  $1.5 \times 1.5 \text{ m}$  rock column within seismic transects. P-waves travel along layer boundaries (Hauck and Vonder Mühll, 2003) which can be different layers of rock mass with different elastic properties or anisotropies caused by macroscopic air-filled faults and joints (Heincke et al. 2006). Therefore, ray density is increased in areas of fracturing in comparison to areas of low fracturing.

To assist with SRT interpretation, and to identify major sub-vertical fractures, faults, and bedding structures, ground penetrating radar reflection surveys were conducted at each seismic transect using a Sensors and Software Pulse Ekko Pro GPR. Three additional GPR transects were deployed around Mueller Hut (GPR 1, 2, 3 in Fig. 3) to evaluate the subsurface persistence of several scarps. They are 30-, 55- and 100-m long respectively. For all GPR transects, stepped measurements were taken at 25 cm intervals along each transect using 100 MHz unshielded antennas. Topographic profiles from RTK GPS surveying were applied to correct for topography, and velocity was evaluated from hyperbola-fitting and common mid-point surveys and applied in Sensors and Software Ekko Project 3 software. Gains were adjusted to enhance weaker reflectors, using a combination of SEC2 and AGC methods. Discontinuities were mapped onto the radargrams, guided by matching discontinuities seen in the radargram with those observed in the field.

Subsurface features were identified to a depth of 15 m within the GPR radargrams and up to 20 m in the seismograms. These penetration depths are deemed adequate for identifying surficial rock mass quality around the ridgeline and Mueller Hut as well as

identifying a potential sliding surface within the headscarp/toppling zone.

### Rock mass characterisation

Descriptions of the rock mass and rock mass characterisation were made for the rockslide and surrounding area. The Geological Strength Index (GSI) was utilised to describe rock mass “blockiness” and the presence of discontinuities within the rock mass following the methodology of Marinos et al. (2005).

### Slope stability modelling

To help evaluate the importance of rock mass anisotropy (i.e. bedding) in influencing the stability conditions and development of the Mueller Rockslide, we used the two-dimensional finite element software RS2 (Rocscience 2019). A cross section equivalent to that shown in Fig. 2 was used to set the topographic boundaries of the model. The assumed geomechanical properties (Table 2) were selected to be representative of greywacke in New Zealand (compilation in Cook, 2001) and conditions observed at the Mueller Rockslide. Equivalent elastic perfectly plastic Mohr-Coulomb strength parameters were estimated using RocLab (Rocscience, 2017). To evaluate the influence of the bedding orientation on the displacement and stability condition at Mueller Ridge, a model with isotropic strength material (no bedding) was compared with a model assuming an anisotropic direction 40° dipping to the west (bedding). The frictional strength along the anisotropy plane was assumed to be 33° using the tilt test results from McColl (2012b). The critical shear reduction factor (SRF; Matsui and San 1992) was calculated to assess the relative stability of both the isotropic and anisotropic models.

## Results

### Rockslide geomorphology

From our mapping, we divide the rockslide and surrounding slope into three major zones, characterised by distinct morphology: (1) a main landside body; (2) a complex headscarp zone of block toppling, block dilation and sliding; and (3) a retrogressive zone with large tension cracks, fractures and small scarps.

#### Rockslide body

The main rockslide body is expressed as a partly disaggregated rock mass that has been moving downwards and outwards into Mueller Glacier Valley (Fig. 4). Extending from 1700 to 1150 m.a.s.l., the surface of the main rockslide body slopes towards the valley

floor at an inclination of approximately 31°; the upper slope averages 29 to 30°, steepening to 37–39° near the rockslide toe. This transition is marked by a lateral moraine extending across the majority of the landslide. Much of the rockslide body is mantled with debris from weathering processes, rockfall, glacial deposits and blocky debris from disaggregation of the rockslide body. Where not covered by debris, the bedrock shows indications of sculpting by glacial or nival erosion (smoothed rock surface and striations), and evidence of brittle deformation (fractures and scarps). Most of the scarps within the rockslide body are down-slope-facing, but in the upper part of the rockslide body there is a low-profile upslope-facing scarp, which is hypothesised to form the downslope edge of a large graben structure (Fig. 4) which was identified in field mapping. The graben structure may represent the separation of the rockslide body from the headscarp zone but has little to no vertical geomorphic expression because it is mostly filled with blocky debris from the collapsing headscarp zone.

A prominent lateral moraine can be traced across the rockslide body immediately above a prominent break in slope 160–230 m above the Mueller Glacier surface (Fig. 4). Up- and down-valley of the rockslide boundary other lateral moraines were identified, some resting at higher and more eastward locations on the slope. It is inferred that the moraine ridges identified in Fig. 4 outside the rockslide boundary are of equivalent (LIA) age to the moraine ridge on the rockslide body. If correct, rockslide movement has displaced the lateral moraine on the rockslide by about 100–130 m horizontally west and 110–120 m vertically down.

The toe of the rockslide body below the LIA trimline is affected by shallower mass movement processes, with an apron of debris having built up at the base of the slope. At the southern end of the rockslide toe, and beyond the rockslide extent, shallow mass movement processes have removed parts of the LIA trimline and moraine altogether.

#### Headscarp and toppling zone

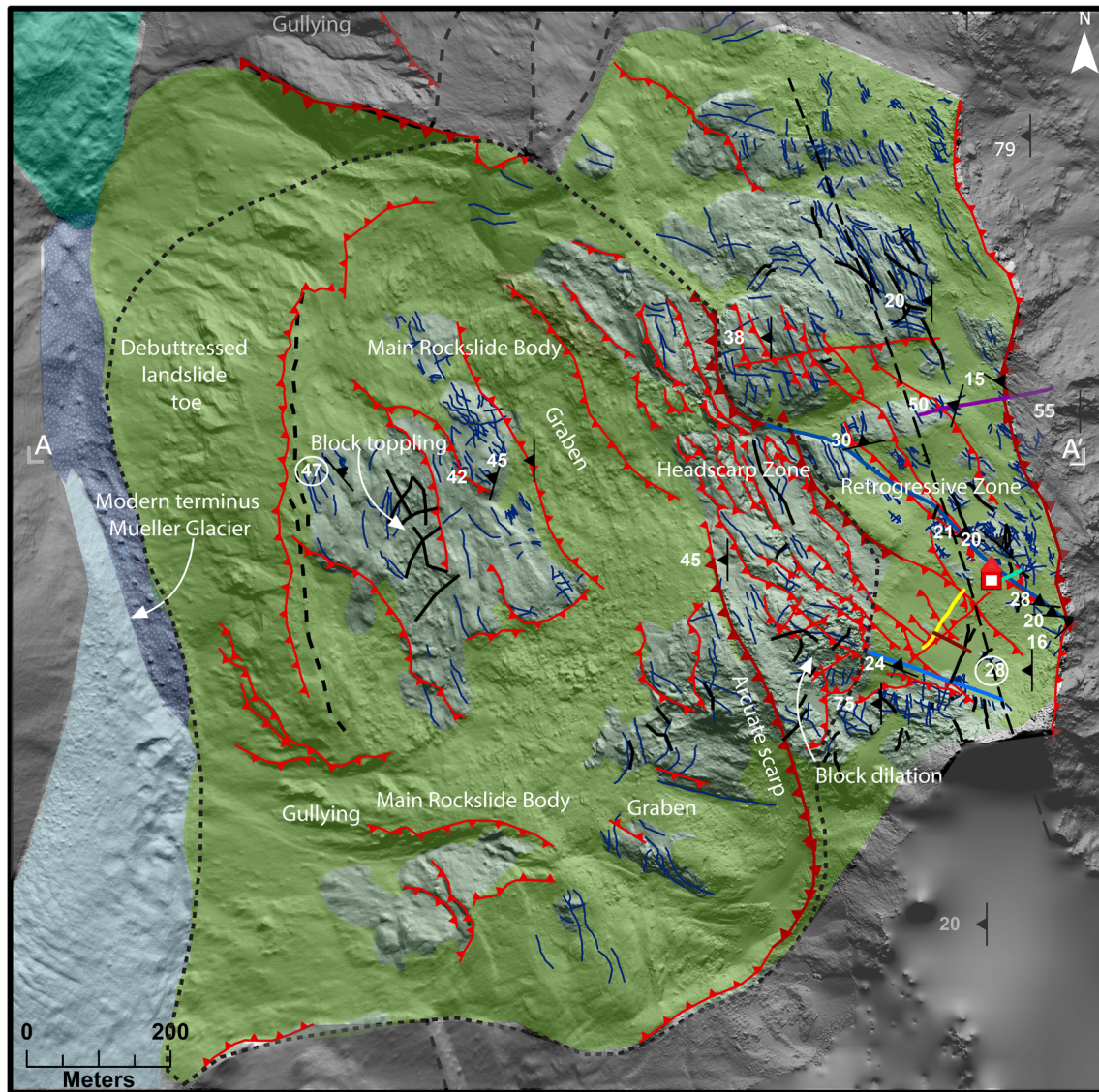
The crown of the rockslide is defined by a network of stepped, discontinuous and echelon scarps that form a wide (200–300 m) headscarp zone extending from 1830 to 1700 m.a.s.l. Slope angle varies from < 30° in areas of intact bedrock to 90° along fractures. Individual scarps have vertical offsets of up to 20–30 m (Fig. 4). The visible cumulative vertical displacement across these scarps is 55–70 m in the northern/upper section of the headscarp and decreases to 30–40 m in the southern part where the scarp transitions into a single arcuate scarp and becomes the southern lateral boundary of the rockslide. Towards the north, the headscarp is less defined but appears to transition into a lateral scarp that defines the northern extent of the rockslide. The lateral scarp is 50–100 m high, and of varying strike, appearing to follow planar pre-existing structures. The stepped scarps forming the headscarp are facilitating forward-toppling of large (up to 140 m long, ~ 0.2 Mm<sup>3</sup> in volume) blocks of rock (Fig. 4). Several incipient block topples/failures are evident from the presence of open cracks. It appears that rock blocks have been breaking up and delivering blocky debris to the main rockslide body.

#### Retrogressive zone

Above the crown (> 1830 m.a.s.l.) the slope gradient decreases to < 10° and is represented by an almost flat-topped ridge heavily

**Table 2** Summary of geomechanical parameters used in the exploratory finite element models of the Mueller Rockslide.

Property	Value
Density	2600 kg/m <sup>3</sup>
Intact rock Young's modulus	35 GPa
Poisson's ratio	0.25
Unconfined compressive strength	80 MPa
Geological strength index	60
mi	11



## Legend

Scree/ Debris	Wide fractures (+1 m)	Kitchener Anticline Hingeline	GPR Transect 1
Bedrock	Fractures	Bedding	GPR Transect 2
Mueller Glacier	Major scarp	Mueller Hut	GPR Transect 3
Frind Glacier	Minor scarp	Landslide outline	Old Hut Transect
Dead Ice	Lateral Moraine		Mount Ollivier Transect
			Mueller Hut Transect

**Fig. 4** Geomorphic map of the Mueller Rockslide. Mapped bedrock (light green) can be seen throughout most of the ridgetop and headscarp but is limited to a central zone with the rockslide. The majority of the rockslide is debris-mantled (darker green). Major and minor scarps are located throughout the rockslide with additional scarps identified and located throughout the ridgetop to the east of the main rockslide headscarp. GPR and SRT transects are located near Mueller Hut and extend generally E-W and NE-SW. At the northern end of the rockslide, Mueller Glacier has almost thinned completely, allowing the Frind Glacier to flow up valley back towards the rockslide. A to A' highlights the location of the cross section shown in Fig. 12. Circled strike and dips are not considered in situ (i.e. have been significantly displacement by landslide movement)

mantled with blocky scree, with patches of exposed fractured bedrock. Fractures vary in aperture from tight to the largest open fracture being over 3 m wide to a depth of at least 7 m. Fracture length varies from several metres long to some fractures that

extend for over 100 m along the ridgeline. Several large tension cracks (without evidence of vertical displacement) are present. These vary in width from 0.2 m wide to 3 m and extend for over 20 m. Smaller tension cracks measured 0.02 to 0.2 m wide and up



to 10 m long. While most fractures have no evidence of shearing, some have evidence of vertical displacement represented by low scarps (Fig. 4). This vertical displacement varies from 0.5 to 2 m, extending for tens to hundreds of metres with down-throw towards the SW and SSW. They are often subtly visible in the field where mantled by debris but are more readily recognised and traceable in the DEM hillshade and aerial photography. Where the scarp travels through bedrock, extensive dilated fracturing occurs with some fractures exceeding 2 m in aperture. The scarps are at a similar orientation to the major scarps making up the headscarp zone below the rockslide crown; for example, the southern-most scarp trends northwest and dips southwest through the northern face of Mount Ollivier before intersecting the headscarp zone (Fig. 4). To the north, two scarps at similar orientation to the southern-most scarp are located on each side of Mueller Hut and converge 100 m north-west of the hut. Both have subtle surface expression but at their point of intersection there is an area of intense fracturing approximately 30 m long, 1-3 m wide and 1-3 m deep before becoming scree filled.

### Rock mass characterisation

The greywacke sandstone is typically weathered orange (lightly weathered, NZGS 2005) with fresh surfaces light grey. Jointing is obvious and quartz veins often fill many open joints with some being over 10 cm wide. Geological strength index (GSI) was used to describe the sandstone rock mass quality as very blocky with good surface which represents a GSI range between 50 and 60. The rock

is indurated and takes several hard hammer or sledge hammer blows to break. Minor seepage could be seen within the main headscarp zone. Siltstone and argillite bedding within the study area is often dark grey, laminated and highly fractured with very small angular blocks. The argillite rock mass is intensely jointed with fair surface condition and can be broken by hand with effort. The argillite rock mass is considered as blocky, disturbed and seamy which corresponds to a GSI of between 30 and 40.

### Discontinuity analysis

Stereographic projections of discontinuity orientations are presented as well as kinematic analysis for planar sliding, wedge and flexural toppling (Fig. 5). Discontinuities are grouped into two structural domains (1) ridgetop/retrogressive zone (Fig. 5) and (2) headscarp and rockslide body zones (Fig. 6) with several discontinuity sets identified within each domain. Identified discontinuities are divided into bedding, joints and faults.

Seven discontinuity sets are identified within the retrogressive zone (Fig. 5a). R1 is a strongly defined bedding set dipping north with an average dip of 30°. R2 is a near vertical joint set trending north-south and dipping predominantly to the west from 80 to 90° although several joints dip steeply to the east. R3 is a minor joint set dipping steeply north at 85°. R4 is a minor joint set striking east-west and dipping at approximately 50° to the south. R5 strikes northwest and dips steeply to the southwest at 75–90°. R6 strikes north-south, similar to R2 but with a shallower dip of 60–70° to the west. R7 strike northwest like R5 but dips east at 70–80°.

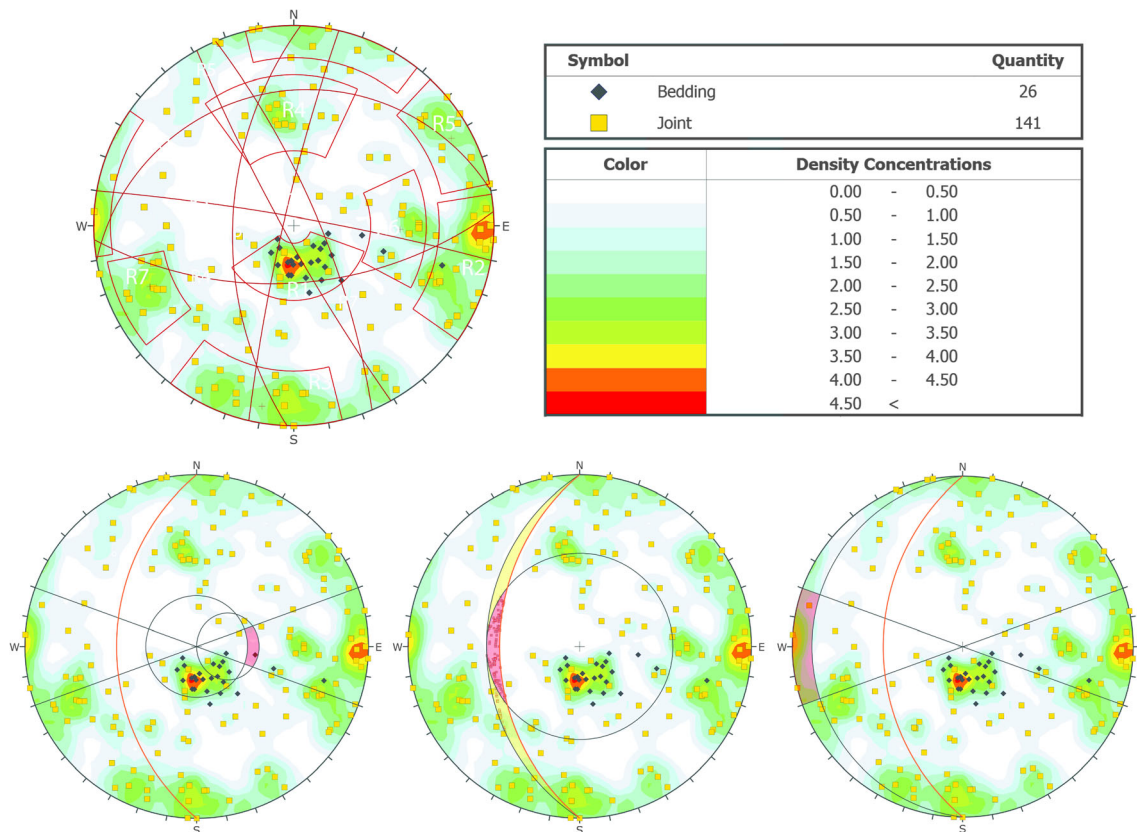


**Fig. 5** (A) Joint sets (R1–R7) and corresponding planes for discontinuities within the retrogressive development zone of the rockslide. Kinematic analysis was completed for planar sliding, wedge and flexural toppling respectively (B, C, D)

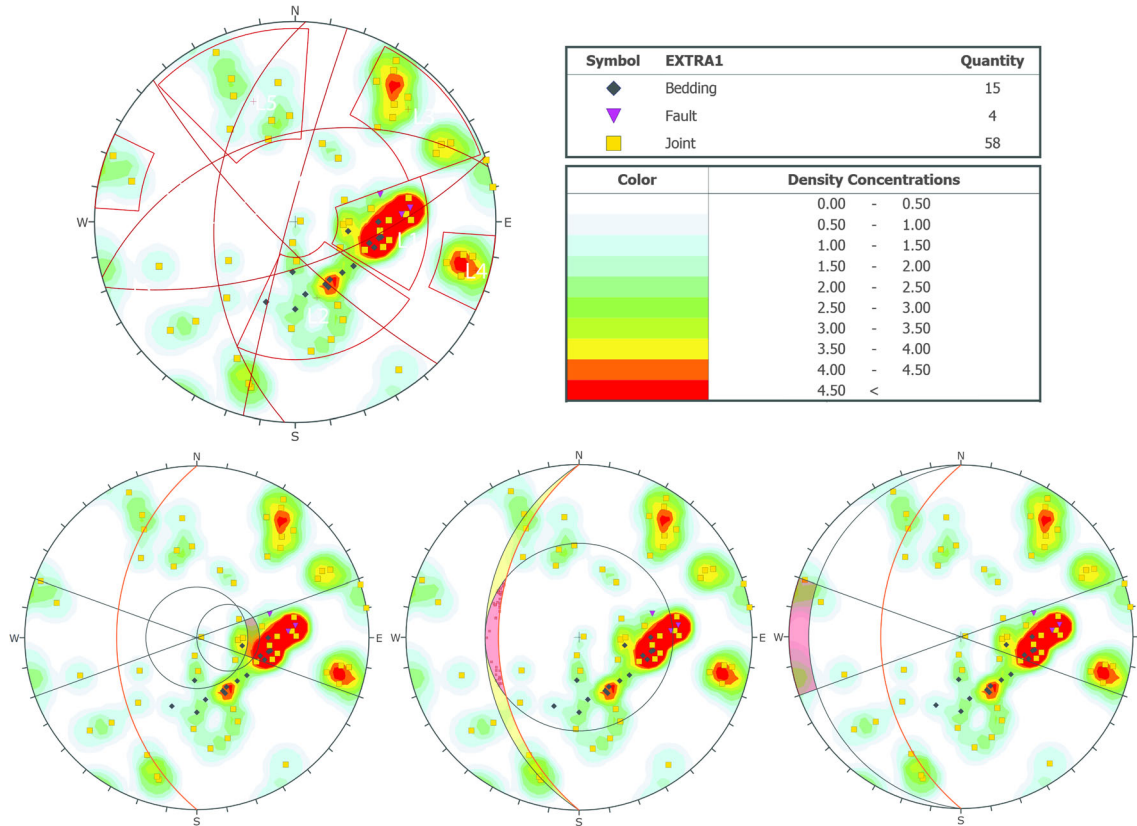


**Fig. 6** (A) Joint sets (L1–L5) and corresponding planes for discontinuities within the landslide and headscarp zone of the Mueller Rockslide. (B–D) Planar, wedge and flexural toppling kinematic analysis respectively

Discontinuities mapped within the rockslide body and headscarp differ from those identified along the ridgeline (Fig. 6a). In total, 5 discontinuity sets are identified. L1 is a predominantly defined by bedding, dipping to the west from 30 to 70° with an average dip of 50°. L2 is a minor joint set again strongly defined by bedding although this set dips to the north-west at approximately 45°. L3 strikes northwest and dips to the south-west at 80°. L4 is an east-west trending joint set, similar to R2 in orientation with joints dipping to the west with an average dip of 80 to 85°. L5 is a minor joint set dipping to the south-east at approximately 80°.

Kinematic analysis was conducted for both domains, to explore potential differences in kinematics between the upper and lower part of the slope. We assessed the potential for planar, wedge, and toppling failure under the following scenario: an empirically derived friction angle of 33° for the mudstone, and a slope dip and dip direction of 40/270. The direction (of 270°) is along the steepest path of the slope and is slightly oblique to the dip direction (~ 285°) of most bedding measurements. Using an average slope angle of 31° (which is below the friction angle of 33°) does not result in kinematic feasibility by planar failure. However, slope angles of up to 39° were measured at the toe, and we evaluate the kinematic feasibility at a slope angle of 40° to provide a conservative estimate that allows some freedom for a potentially lower friction angle.

For the retrogressive zone (Domain 1), the kinematic analysis shows that potential for planar failure is minor (Fig. 5b) with only one bedding point (3.8% of total bedding measurements) falling within the failure envelope. Wedge failure analysis shows the

potential for failure along the intersection of R3–R6 and R4–R6 joint sets (Fig. 5c); however, the failure envelope falls just outside the definitive intersection of these joint sets. Flexural toppling analysis shows potential toppling along the R4 eastward dipping discontinuities (Fig. 5d).

For Domain 2, the kinematic analysis showed marginal potential for planar sliding although no discontinuities fall in the failure window; several L1 discontinuities are at the margin or just outside of the failure window. Wedge failure analysis shows potential for L1–L3 and L1–L5 intersections within or just outside the failure envelope (Fig. 7c) (2.2% within failure window). Flexural toppling analysis shows L4 discontinuities falling within the failure envelope when the slope angle is 40° (Fig. 7d) (1.3% total discontinuities and 16.7% of L4 discontinuities)

#### Subsurface data: SRT and GPR

##### Mueller Hut transect (T1)

The Mueller Hut transect (T1) extends from 100 m east of Mueller Hut in the upper ridge to the rockslide crown for a total length of 500 m (Fig. 4). There are three distinct velocity layers recognisable along the seismic transect (Fig. 7). The near-surface p-wave velocity layer (0.5–0.95 km s<sup>-1</sup>) is predominantly located within the first 100 m of the transect to a depth of 5 to 7 m below ground level and from 140 to 380 m to a depth of 3–5 m. A second, faster, velocity band (0.95 to 1.7 km s<sup>-1</sup>) is observed predominantly from 140 to 380 m, through localised areas of bedrock outcrop and in the final 150 m of the transect towards the rockslide

crown. The third and fastest velocity band ( $> 1.7 \text{ km s}^{-1}$ ) is found between 400 and 480 m along the transect.

Fracture density results show high values in the first 100 m of the transect as well as between 140 and 280 m, coinciding with the low p-wave velocities outlined above and areas of blocky debris seen on the surface. Fracture density decreases rapidly with depth under areas of scree and in areas of bedrock from 30–50% in scree zones to 10–30% in bedrock and the underlying rock mass. The last 150 m of the transect shows lower fracture densities particularly in relation to the debris-mantled ridgeline.

Ray density analysis shows the percentage of rays per  $1.5 \times 1.5 \text{ m}$  grid spacing with high ray density indicating the presence of linear features or discontinuities. In the first 100 m, of the transect, ray density appears to be related to scree and suggests an absence of large, persistent fractures within the bedrock. Farther down the transect, high ray densities are detected from 140 to 280 m with increased ray density at the surface and moderate density at depth to  $\sim 30 \text{ m}$  indicating the presence of large, persistent structures (black arrows in Fig. 7b). High ray density also indicates a large persistent fracture at 430 m is also indicated by high ray density.

The corresponding GPR profile for transect 1 is 400 m long, extending almost to the rockslide crown. Evidence of bright reflectors which coincide with areas of bedrock at 100–200 m are interpreted as bedding planes. Reflectors with a similar signature can be seen at depth at 175 m along transect and at 380 m (Fig. 7c, d). The first 210 m of the transect which bypasses Mueller Hut also shows extensive orthogonal fracturing with apparent dips to the east and west. A highly fractured zone from 140 to 210 m along the transect is marked by significant fractures which extend for  $\sim 8 \text{ m}$  through the GPR profile. A scarp identified in the geomorphic mapping and in the field at 140 m is hard to identify within the GPR transect due to both being oriented in a north-west direction however there is evidence of shear planes and displaced bedding around 140 m.

From 210 to 310 m, fractures appear to dip predominantly westward as the transect moves towards the crown of the Mueller Rockslide. A highly fractured zone can be seen between 220 and 245 m (Fig. 7c) which coincides with where the two minor scarps either side of Mueller Hut intersect and with several large fractures identified on the geomorphic map. Bright linear reflectors identified between 290 and 320 m are interpreted as bedding. From 310 m, fractures have an apparent dip to the east, coinciding with the transition to block toppling as the transect nears the headscarp.

#### Mount Ollivier transect (T2)

The Mount Ollivier transect (T2), located south of Mueller Hut, is 200 m long extending from below Mount Ollivier to the rockslide headscarp (Fig. 4). Two p-wave velocity layers have been identified within the Mount Ollivier transect (Fig. 8). The first ( $0.5$  to  $0.95 \text{ km s}^{-1}$ ) is located mainly in the top 10 m through the entire transect extending to 15 m depth from 120 to 160 m (Fig. 8b). The second, and faster, velocity band ( $0.95$  to  $1.7 \text{ km s}^{-1}$ ) is found from 40 to 160 m. A third velocity layer ( $> 1.7 \text{ km s}^{-1}$ ) can be seen in isolation from 25 to 40 m.

Fracture density analysis shows the majority of the top 7 m of the transect shows fracture densities greater than 40% with this decreasing to 15–30% underneath the upper scree areas. At 30 m low fracture densities of less than 10% are seen, corresponding with mapped bedrock along the surface of the transect. Ray density analysis shows an area with extensive and persistent fractures at 110 to 190 m (black triangle, Fig. 8b).

The Mount Ollivier GPR transect shows an apparent dip to the west of several strong reflectors (Fig. 8c). At 55 m and 150 m are east-dipping reflectors which extend for over 10 m depth in the GPR profile. A similar albeit small feature is identified at the end of the transect between 160 and 180 m within 20 m of the previously identified rockslide headscarp. Four strong sub-horizontal reflectors are identified in the eastern most extensive feature from 22 m to 55 m, interpreted as (argillite) bedding, consistent with outcrop observations; similar but more steeply-dipping reflectors are identified between 120 and 160 m. A large tension crack (Fig. 8c, e) extends throughout the transect as well as extending for a total of 40 m to the north (Fig. 8a). An extensive shear plane can be seen from 110 m which extends throughout the GPR transect and is represented at the surface by a continuous 1–2 m southwest dipping scarp (Fig. 8c, d).

#### Old Hut transect (T3)

The Old Hut transect (T3) is located to the north of Mueller Hut extending for 200 m from the eastern headscarp through the ridge-line (Fig. 9). P-wave velocity analysis has identified 3 dominant velocity bands. The first, and slowest, velocity band ( $0.5$  to  $0.95 \text{ km s}^{-1}$ ) is found through the upper 1–4 m depth of the majority of the transect particularly in areas mapped as debris or scree. The second band ( $0.95$  to  $1.7 \text{ km s}^{-1}$ ) is at 30 m from 0 to 12 m deep, at 70 m from 2 to 15 m deep and 160 m distance from 5 to 17 m deep (Fig. 9b). The third and fastest p-wave velocity band ( $> 1.7 \text{ km s}^{-1}$ ) can be found from 0 to 10 m, 40 to 60 m and 80 to 150 m.

Fracture density patterns show fracture zones at 30, 70 and 160 m distance display very high fracture densities of greater than 30% with the fracture zone at 70 m exceeding 50% fracture density (Fig. 9b). This fracture zone is characterised by fracture widths at the surface of greater than 0.5 m. At 150 m, both methodologies identified a large fracture zone which also corresponds to high ray densities that the existence of persistent fractures.

GPR results again have highlighted an extensive network of fracturing. Due to the blocky surface in this area and lack of outcrop, identified fractures are mainly isolated to the first 100 m of the transect near the main eastern scarp, and to an isolated but highly fractured bedrock zone from 130 to 170 m (Fig. 9e). The most extensive zone of fracturing is located from 25 to 70 m marked by several crossed eastward and westward dipping fractures and one major failure zone (Fig. 9e; red lines) which extends through the GPR profile, marking the headscarp of the eastern rift/graben. Although graben is block-filled, vertical displacement of  $\sim 5 \text{ m}$  is estimated from the GPR profile, consistent with the height of the graben scarp. Minor fracturing from 90 to 130 m in the GPR profile is hidden in the field, the area covered with blocky debris. Strong gently-west-dipping, reflectors through this zone are interpreted as bedding which extends from 85 to 135 m along the transect. Bedrock outcrop from 130 to 170 m largely consists of minor superficial fracturing with fractures appearing to only extend for several metres. However, from 155 to 165 m, there are two very large parallel vertical dislocations extending through the radargram and marked at the surface by two large ( $\sim 30 \text{ m}$  long and 0.5 m to 3 m wide) open fractures with a bedrock wedge in between. The wedge sits 2 m lower than the surrounding bedrock and the surfaces corresponding to the dislocations extend for at least 10 m deep in the radargram. There is no obvious vertical displacement between each side of the wedge (i.e. no scarp).

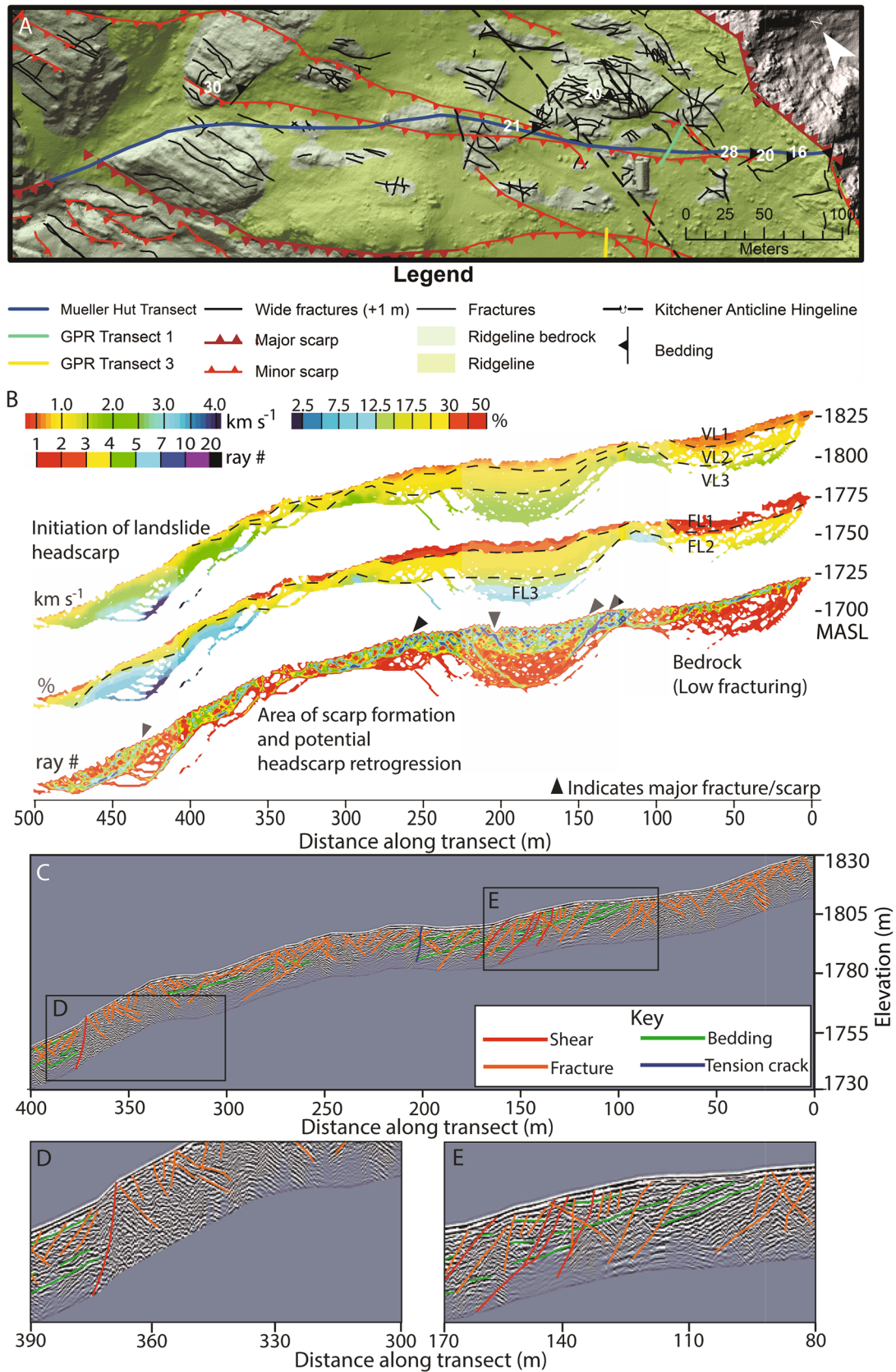


**Fig. 7** Mueller Hut seismic transect (T1). (A) Geomorphic map of the transect. (B) SRT transect consisting of P-wave velocity, fracture percentage and ray density. High ray density indicates clustering of linear features (black arrows) indicating potential scarp or fracture development. (C) GPR transect for 0–400 m. (D) Beginning of the block toppling and headscarp zone. (E) GPR directly adjacent to Mueller Hut (105 m)

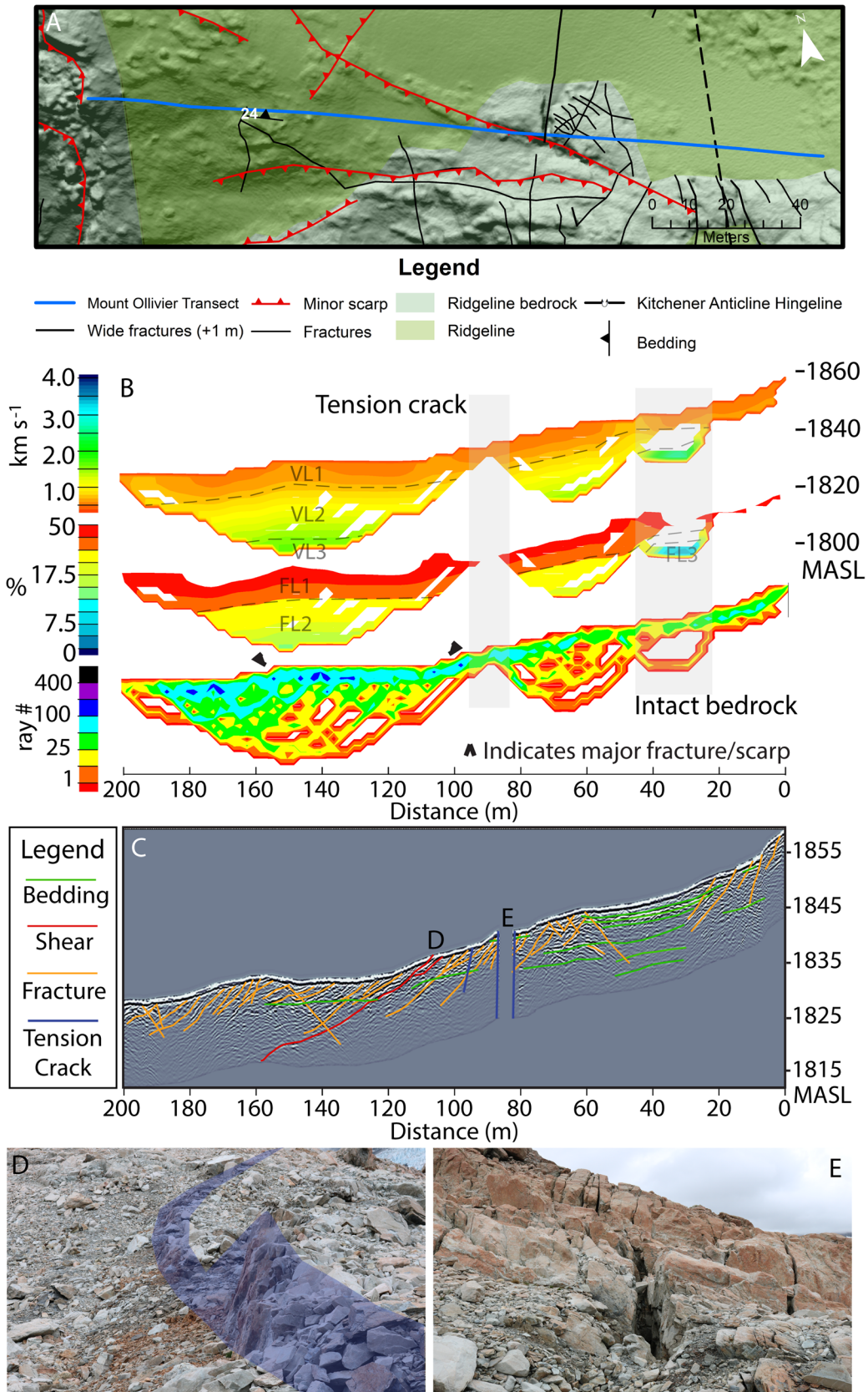


**Fig. 8** SRT and GPR for the Mount Ollivier Transect. (A) Geomorphic map of the Mount Ollivier transect. (B) SRT showing in order p-wave velocity, fracture percentage and ray density. (C) GPR with identified bedding, fractures, shear planes and tension cracks. (D) Scarp associated with the mapped shear surface within the transect dipping to the southwest (left in the image). (E) Large dilated tension crack within the transect

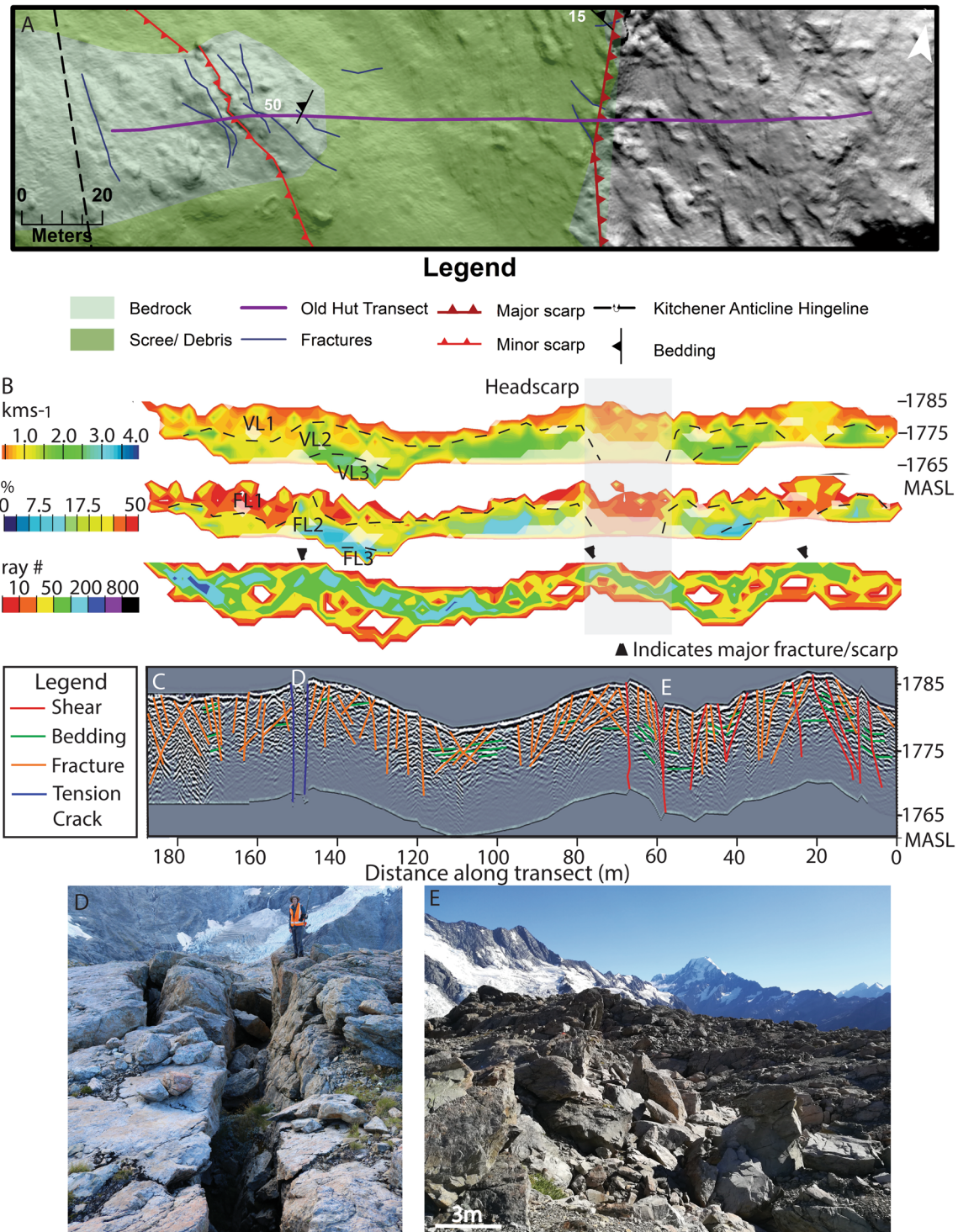


**Fig. 9** Old Hut seismic transect. (A) Geomorphic map of the transect and surrounding area. (B) SRT showing P-wave velocity, fracture percentage and ray density. (C) GPR. (D) Large tension crack 150 m along the transect. (E) Headscarp for the eastern slope failure which is partly obscured by block fill

#### Additional GPR transects

Radargrams from the three additional GPR transects, in proximity to Mueller Hut, are presented in Fig. 10. Transect 1 reveals the scarp identified at the surface is associated with two near vertical shear surfaces that extend through depth of the transect (Fig. 10a). Several near vertical fractures can be identified within the graben

between the two shears while fractures outside the graben appear to have a shallower dip.

Transect 2 crosses a large north-south trending scarp as well as the large tension crack identified in the Mount Ollivier seismic transect. The tension crack appears to split into at least two large fractures at depth (Fig. 10b). Distinct bedding can be seen dipping

to the right (west) before being displaced by an obvious shear surface which corresponds with the scarp at 45 m.

Transect 3 shows mapped scarps in the area south of Mueller Hut correspond with shear surfaces at depth. In total, 4 scarps were identified with all scarps corresponding with shear surfaces at. Additional 3 shear surfaces were identified which do not correspond to scarps at the surface (Fig. 10c). Determining the depth of these shear surfaces was difficult due to the poor quality of the GPR in the final 50 m of the transect; however, all extend to at least 10-m depth.

### Slope stability modelling

The calculated critical SRF for the isotropic model was greater than the one obtained for the anisotropic model. More importantly, the displacement pattern at the critical SRF model is on the east side of Mueller Ridge for the isotropic model whereas it shifts to the western (i.e. Mueller Rockslide) side when the bedding anisotropy is considered (Fig. 11). This numerical modelling assessment provides simple but useful support for the idea that the Mueller Rockslide is structurally influenced by the bedding. However, neither model produced a SRF approaching a critical value of 1, suggesting that the rock strength parameters used or the bedding orientation were inappropriate (i.e. too strong), or groundwater or other processes not included are important for bringing the slope to a critically stable state. Additional models considering a wider range of strength parameters, the influence of more subtle structural weaknesses (e.g. discontinuity sets) and potential triggers (groundwater and seismicity), will be investigated in the future.

## Discussion

### Comparisons between SRT, GPR and geomorphic mapping

Geophysical surveys including SRT and GPR have become common place in recent decades for quantifying rock mass qualities and discontinuities of rock slope failures (Heincke et al. 2010; Bekler et al. 2011; Meric et al. 2005). SRT and GPR have been previously combined in rock cavity identification or in the study of smaller fracture zones (De Giorgi and Leucci 2014; Heincke et al., 2006). Herein, we further demonstrate the utility of these two techniques for confirming the presence and subsurface continuity of deformation indicated at the surface by scarps, and for supporting geotechnical mapping of fractures into the subsurface, especially where bedrock is obscured by debris. In addition, we show how SRT can be used to reveal changes in fracture density at depth, as well as revealing the thickness of surficial materials overlying bedrock.

This study has shown a strong relationship between areas of increased fracturing (high fracture percentage) in the SRT with fractures identified within the GPR. Areas of low p-wave velocity ( $< 2.0 \text{ km s}^{-1}$ ) and high fracture percentage ( $> 30\%$ ) often were located in areas with numerous fractures. In particular, several shear surfaces were distinguishable within the SRT in the Old Hut and Mueller Hut transects, consistent with field mapping (scarp identification) and GPR. For the Mueller Hut transect, ray density analysis showed this particularly well as the transect passed through a more intact bedrock zone, allowing for the difference between intact and highly fractured bedrock to be seen.

Inclusion of the GPR also allowed for the identification of bedding planes which were not readily apparent from the SRT

data; this information was useful for identifying shear surfaces at depth and linking them to mapped scarps at the surface. While the GPR was also useful for detecting discontinuities, GPR is not effective at imaging feature parallel to the radar transect (i.e. vertical features along the transect). We believe tension cracks and other vertical discontinuities within the GPR data are under-represented. Combining the two methods (SRT and GPR) helps to minimise some of the shortcomings of the individual techniques and provided richer results. This enabled a more comprehensive assessment of all structural features throughout the surveyed area and the methods complimented each other to provide a view of broader rock mass quality and the relationship to bedding, fractures and shear planes. Overall, the three techniques (GPR, SRT and field mapping) were consistent and complimented each and here they have confirmed the presence of major open fractures, and vertical deformation along features consistent at the top of the rock slope. The kinematic analysis suggests that planar failure along bedding is unlikely here, and instead the geophysics indicates that this deformation is being accommodated by sub-vertical joints, likely the same ones controlling the headscarps. This suggests that the rock mass of the upper part of the rock slope is facilitating retrogressive enlargement of the rockslide.

Access and safety made it unfeasible to extend the geophysical surveys across the entire rockslide, and the depth of penetration by SRT was limited by use of mechanical means of seismic signal generation (i.e. sledge hammer). Nonetheless, this study demonstrates the utility of these techniques on large rock slope failures and DSGSDs, if they can be safely deployed and especially if larger seismic sources can be generated (e.g. dynamite).

### Structural controls on rockslide morphology

Geomorphic mapping, SRT and GPR have identified an extensive fracture network at the Sealy Range. The discontinuity sets in Figs. 5 and 6 are equivalent with fractures commonly associated with folding (Price and Cosgrove 1990). Specifically, discontinuity sets closely align with fractures oriented parallel, perpendicular and orthogonal to an anticline (Fig. 12).

Excluding bedding, discontinuity sets identified along the ridgeline align parallel (R<sub>2</sub>, R<sub>6</sub>) and perpendicular (R<sub>3</sub>, R<sub>4</sub>) to the main anticline hingeline (Figs. 5 and 12) and are classed as extensional joint sets. R<sub>5</sub> and R<sub>7</sub> are orthogonal fractures in the retrogressive zone and are classified as shear fractures. Discontinuity sets within the landslide zone are predominantly orthogonal to the main hingeline and dip to the northwest (L<sub>2</sub>), southeast (L<sub>5</sub>) and southwest (L<sub>3</sub>) and are interpreted as shear fractures.

Preconditioning and morphology of the Mueller Rockslide has been strongly controlled by its location on the dip slope of the Kitchener Anticline. In fact, without structural controls and anisotropy, failure of the hillslope would only occur to the east as indicated by modelling (Fig. 11). Headscarp morphology has strongly aligned with the L<sub>3</sub> and L<sub>4</sub> fractures (Fig. 12) in a northwest–southeast direction with the steep dips of the fractures accounting for the occurrence of block toppling in this area. These joint sets also align with the newly mapped scarps developing along the ridgeline (R<sub>5</sub> and R<sub>7</sub>; Fig. 12) which appear to be facilitating downslope movement of the upper ridge. They appear to act as rear-release structures, similar to what has been previously observed by Brideau et al. (2009) at the Hope slide in British Columbia and the Randa Rockslide in Switzerland. Continued

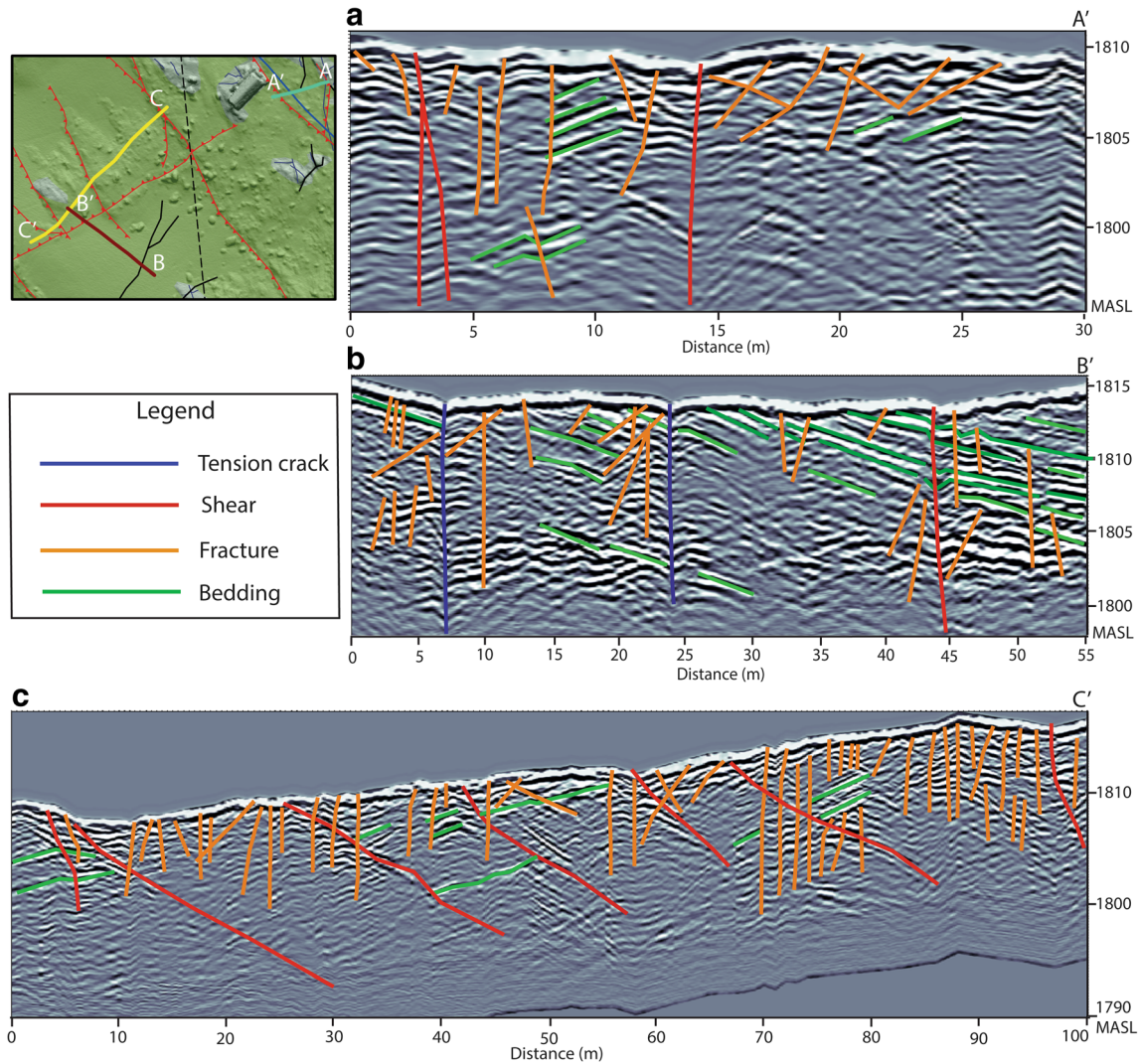


**Fig. 10** GPR transects from the Mueller Hut area. (A-A') Transect 1 going NE-SW approximately 20 m from Mueller Hut. The two shear features identified in the left of the image are considered to be the eastern most scarps for the rockslide retrogressive zone. (B-B') Transect 2 going E-W through the northern limit of a large tension crack. (C-C') Transect 3 going N-W through several large shear features directly south of Mueller Hut

block toppling and rockslide movement has steepened this headscarp zone, allowing for the potential for daylighting of several joint sets and the increased potential for wedge failure and block toppling as indicated in the kinematic analysis (Fig. 6). The north-south oriented R2 and R6 joint sets may also be acting as a minor rear-release mechanism, resulting in the formation of large tension cracks above the headscarp. Lateral release structures are also essential for allowing the rockslide to develop (Brideau et al., 2009). Several east-west oriented releasing scarps were identified (R3 and R4; Fig. 12) particularly to the north-west of Mueller Hut and to the south-west of Mueller Hut above the arcuate headscarp (Fig. 4). The importance of these rear and lateral release structures is highlighted by Brideau and Stead (2012) who demonstrate that persistence of these release surfaces along with their orientation relative to the slope dip direction are essential for controlling rockslide failure initiation as well as rockslide morphology.

The inability to investigate the deep subsurface of the rockslide body has meant that little is directly known about the rockslide

failure surface. Instead, we make assumptions on the failure surface based on scarp and shear surface morphology resolved from the ridgeline seismic transects, observations of rock type and rock mass quality, and discontinuity mapping. The failure surface is assumed to be along bedding (weak argillite layers), consistent with GPS survey data shows that movement in a down-dip direction ( $285^\circ$ ) rather than a downslope direction ( $270^\circ$ ) in the central rockslide (McCull 2012b), and supported by the stability modelling (Fig. 11). However, kinematic analysis indicates simple planar failure marginal or oblique to the slope direction as only one bedding measurement fell inside the failure window (Figs. 6 and 7), consistent with the observation that measured dip of bedding is steeper than the slope of the rockslide. While this makes daylighting of a failure surface along bedding unlikely, there is very little known of the orientation and condition of bedding at the toe of the slope. It is feasible for bedding to fold back into a different structure (e.g. syncline) at the toe and we observe bedrock on the opposite side of the valley appears lithologically and structurally



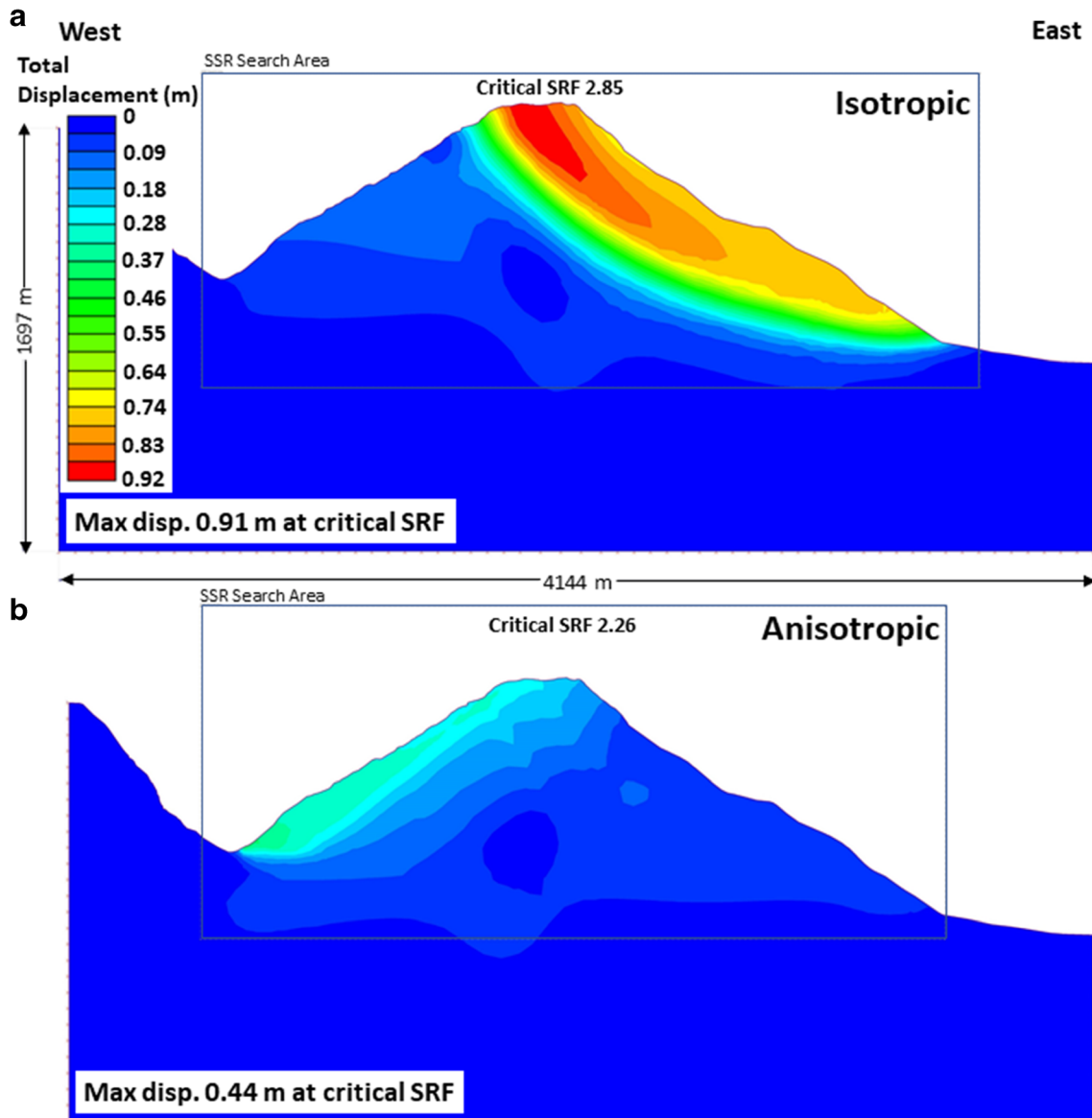


**Fig. 11** Total displacement magnitude across Mueller Ridge at the critical strength reduction factor for an (A) isotropic and (B) anisotropic models. Location of the cross section is equivalent to the one shown in Fig. 2

different. Consequently, bedding may curve into the slope face at the toe of Mueller Rockslide, facilitating kinematic release and sliding along bedding into the valley (Fig. 13a). Alternatively, movement may be accommodated at the toe by ductile deformation (buckling; Fig. 13b) or release along one or more fractures (Fig. 13c).

While toe buckling by ductile processes occurs in the Southern Alps within the highly anisotropic schist (Ridl et al. 2017), this process is less likely to occur in the high strength brittle greywacke. Finite element modelling with the assumed bedding orientation suggests a low failure potential with a high SRF of 2.26 for the western rock slope with displacement of only 0.44 m at that SRF. We therefore suggest that if bedding orientation does not permit kinematic admissibility, breakout along fractures that step across bedding is a more likely scenario. We observe fractures

stepping and shearing across bedding at the top of the slope. GPR and SRT (Mueller Hut transect) show shearing across bedding, facilitated by the joint sets in the retrogressive zone, and at the top of the headscarp where the identified scarp dips near vertically through bedding. Stepping across bedding may in fact be a characteristic feature of the whole failure surface, creating a stepped failure surface connecting planes of weakness (i.e. bedding). Stepped sliding planes have been identified in other large rock slope failures (Oppikofer et al. 2011; Sturzenegger and Stead 2012; Tannant et al. 2017). Ultimately, failure of the rock slope may be accommodated by a combination of geological structure (bedding) and rock mass conditions (joints), both of which are influenced by the Kitchener Anticline.

While the Mueller Rockslide has previously been described as a DSGSD (McColl and Davies 2013), observations from field work

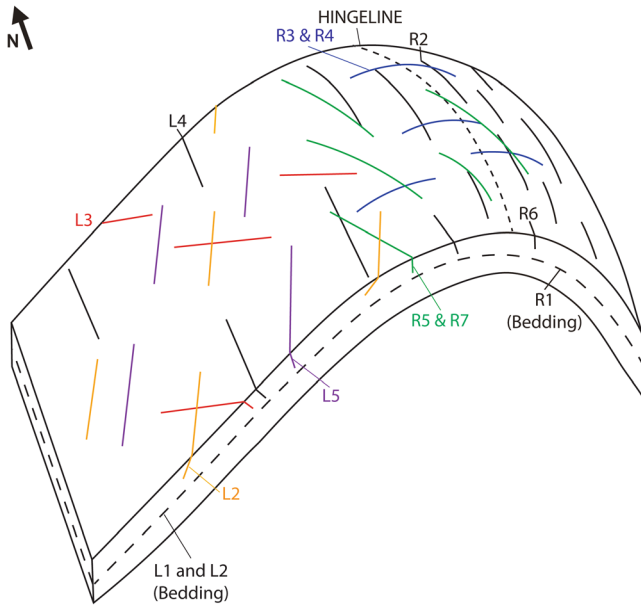


**Fig. 12** Primary discontinuity sets seen within the Sealy Range and northward plunging Kitchener Anticline. Adapted from Price and Cosgrove 1990

and geophysical surveys indicate the slope failure does not display many of the normal attributes seen in DSGSDs. Only a single uphill facing scarp (on the landslide body) was identified, which are normally typical of DSGSDs. Instead, we see a discontinuous but clear set of normal scarps defining the crown. As well, while a bedding failure surface has not been confirmed, movement direction down-dip indicates failure along bedding is feasible. Therefore, we propose that the Mueller Rockslide can be better described as a rock compound slide. As defined by Hungr et al. (2014), rock compound slides are those which form along several planes or a disconnected sliding surface and must undergo some internal deformation to allow movement. Continued internal deformation and weakening of the rock mass (in our case mostly at the toe) may eventually lead to rapid failure. Rock compound slides often have a steep main scarp that cuts through the rock mass (in our case across bedding and along joint sets), and connects to the failure surface.

In summary, structural controls such as bedding and rock mass properties (i.e. joint sets) likely influence the failure mechanism and together explain the rockslide morphology, observed deformation of the rock mass, and why the slope has not yet failed catastrophically. Future work will include stability modelling to test these ideas and explore further the relationship between the observed morphological structures, movement of the slope, and the geological controls.

#### **Rockslide development towards rapid failure**

Slow moving rock slope instabilities can transition to rapid and catastrophic failures (Pánek et al. 2011c; Kilburn and Petley 2003; Geertsema et al. 2006). While assessing the temporal evolution of the Mueller Rockslide has not been the focus of this research, the data collected here can allow a qualitative assessment of whether the Mueller Rockslide could accelerate and fail rapidly, either

overtime as a progressive failure or through an external trigger like strong earthquake shaking.

The evolution of large rockslides towards rapid failure is an important avenue of landslide hazard research (Hungr 2007). Several studies (e.g. Glastonbury and Fell 2008a, 2008b, 2010; Eberhardt et al. 2004; Crosta and Agliardi, 2003) have attempted to identify key structural and geomechanical properties commonly found in rockslides which transition to catastrophic failure and found several common factors, which can indicate potential for catastrophic failure. Common characteristics include a high strength rock mass that facilitates failure en masse rather than smaller slope failures from highly disaggregated rock masses, loss of toe buttressing support, and strongly defined lateral margins (particularly important for deep rockslides) which lie normal to anisotropy (Glastonbury and Fell 2010, 2008b). As well, first-time failure as opposed to those experiencing reactivation are more likely to progress to rapid failure. In contrast, slow moving landslides, which do not progress to rapid failure more often occur in weak, disaggregated rock masses and in slopes where the basal rupture surface angle is less than the residual friction angle (Glastonbury and Fell 2008a).

Our observations show that the Mueller Rockslide has some characteristics in favour of catastrophic failure and others against. GSI values from rock mass characterisation of 50–60 for sandstone and 30–40 for argillite are low to fair, possibly suggesting disintegration rather than failure en masse. However, while the rockslide is clearly fractured, it occupies the entire slope from toe to ridge crest and extends for about 1 km along the ridge, suggesting it is failing as a large mass. The slope has clearly been debuttressed, as a result of thinning of the Mueller Glacier, but has likely undergone erosion by the glacier too, explaining the steepened section of hillslope below the break in slope of the LIA moraine limit (Fig. 13). Lateral restraints are identified within the kinematic analysis (R3 and R4 discontinuity sets) and lie normal to anisotropy (perpendicular to bedding) which is a characteristic of potential rapid failure. While the Mueller Rockslide is currently unstable (indicated by movement data; McColl, 2012b), it is probably not a first time failure, i.e. sliding surface is at residual strength as the rockslide may have been moving for decades to centuries. Displaced lateral moraine shows movement has been ongoing for a significant period of time without yet accelerating to catastrophic failure. This magnitude of displacement, however, suggests that the friction angle of the rupture surface is likely to be at residual values ( $< 33^\circ$ ), and this is considerably less than the dip of the bedding assumed to be the sliding surface (which is a characteristic of rapid failure). Putting some of these conditions together and following the decision tree of Glastonbury and Fell (2008a) for an internally sheared, compound slide, the probability of very rapid to extremely rapid velocity for the Mueller Rockslide is between 55–65%. The upper value represents the case of a rapid external load (e.g. a strong earthquake). Under this decision tree scenario, we assume that the failure surface is at residual strength (i.e. a through-going, well-developed failure surface extending to the toe); if not at residual strength yet, the probabilities increase to 80–90%. The gradual development of a through-going failure surface at the toe, by connection of fractures and breakage of rock bridges, may represent progressive failure of this slope; this could allow the transition to catastrophic acceleration.

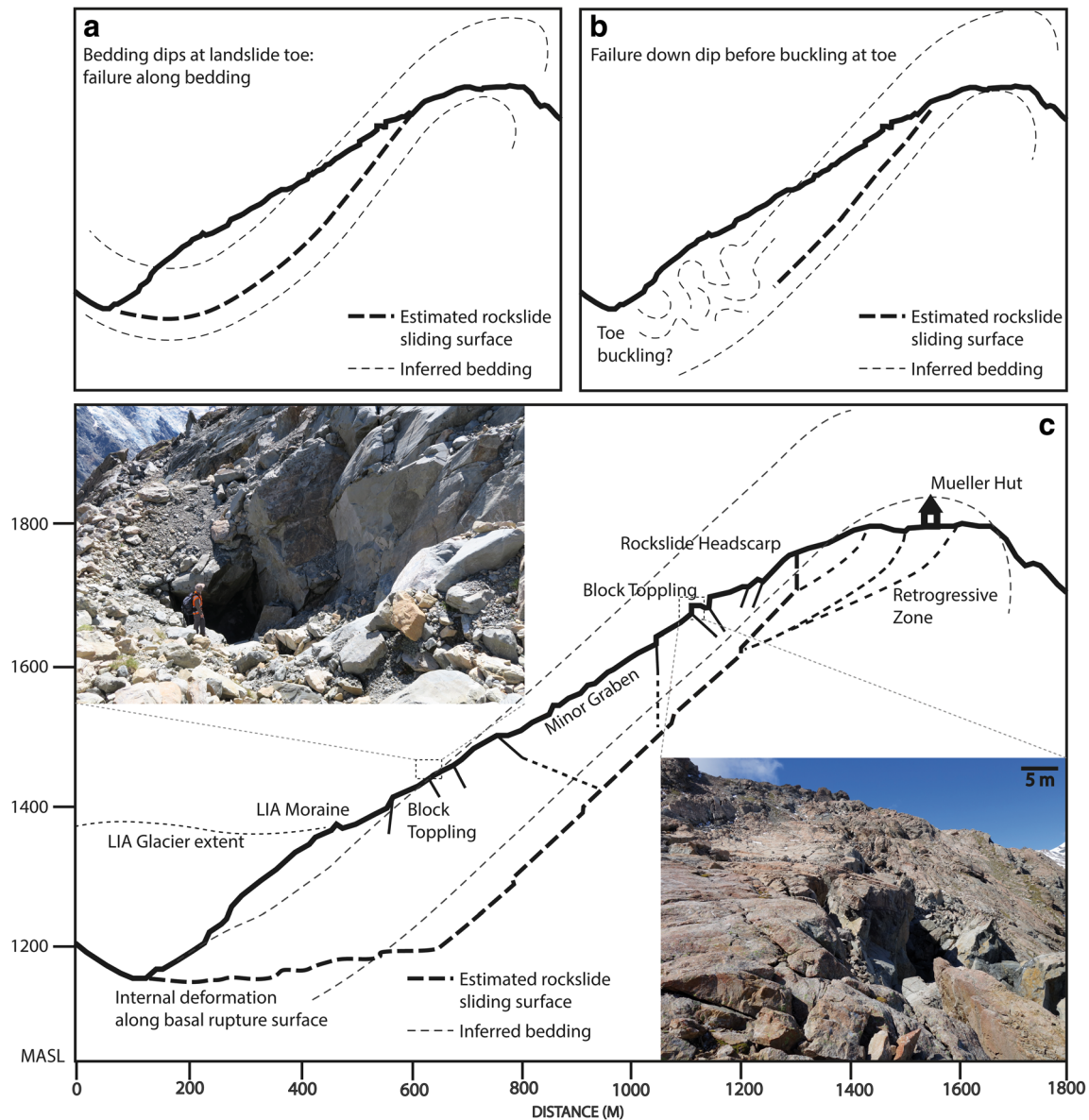


**Fig. 13** Cross section and models of the Mueller Rockslide. (A) Bedding inferred to dip into valley allowing for kinematic release and failure along bedding. (B) Failure along bedding and movement accommodation by ductile deformation and toe buckling at base of slope. (C) Stepped failure approximately down-dip with deformation at toe accommodated by release along fractures. Top image shows block toppling in the lower rockslide (looking north). Bottom image shows the main headscarp and blocking toppling (looking south). Given the height of the headscarps (30 m), plus the identification of a zone of retrogressive development extending 150–200 m east of the headscarp, we assume rockslide thickness to be several tens of metres deep near the top of the rockslide. An increasing thickness downslope is inferred from the observation that bedding dips at a steeper angle than the rockslide slope

These results appear to contradict the simplified modelling results presented in Fig. 11 which indicates failure to be unlikely. However, this model does not account for the influence of toe debuttressing, seismicity and ground water fluctuations. While failure along bedding is feasible, our results indicate it will not occur without external forcing, or through progressive loss of strength. Similar results have been seen within the Moosfluh Landslide and other rock slope instabilities surrounding the Aletsch Glacier. Grämiger et al., 2017 and Glueer et al. 2019 show incremental damage associated with repeat glacier cycles play a significant role in gradually weakening rock masses. In addition, while glacier debuttressing has been identified as a preparatory

factor for many alpine rock slope failures, in the latter stages of retreat glacier ice can induce viscous flow in unstable rock slopes through deformation (McCull and Davies 2013).

Future investigations on kinematics and movement history may provide insights on the relationship between movement and environmental drivers (e.g. pore-water pressure) and external forcings (e.g. seismic shaking). Additional modelling is required to assist in the determination of rockslide failure potential.

### Conclusions

This paper summarises a combination of field mapping, fracture mapping, kinematic analysis and geophysical methods to present

the structural controls and preconditioning factors of Mueller Rockslide. An extensive fracture network throughout the Sealy Range in proximity to the rockslide as well as several scarps above the main rockslide headscarp was newly identified. SRT and GPR have been successfully combined and show extensive fracturing to at least 10 m depth as well as the presence of several shear planes that coincide with mapped scarps at the surface. Several large tension cracks have also been identified above the main rockslide headscarp. The identification of several scarps and tension cracks indicates retrogressive development of the rockslide into the ridgetop.

Kinematic analysis was performed for discontinuities within the rockslide and ridgeline areas. There is a low feasibility for planar sliding and an increased feasibility for wedge and toppling failure was identified through the headscarp and ridgetop. Although there is a limited feasibility for planar sliding, the movement direction of the rockslide is down-dip ( $285^\circ$ ) as opposed to downslope ( $270^\circ$ ), suggesting an influence of bedding, further supported by our stability modelling. We therefore estimate the rockslide is moving along a stepped, discontinuous sliding surface along and through the interbedded argillite and sandstone.

This research shows the formation of the Mueller Rockslide has been strongly influenced by the folding of Kitchener Anticline with failure controlled by bedding angle and orientation and the presence of joint sets commonly associated with anticline formation. While slow moving, the Mueller Rockslide exhibits some features commonly identified within rock slopes that transition to rapid, catastrophic landslides. A strong and predominantly intact rock mass as well as the presence of strongly defined lateral release structures increase the potential for rapid failure.

Future work should focus on identifying key triggers for rockslide movement and investigate the development of the rockslide through monitoring, modelling and cosmogenic dating. The investigation of potential seismic and hydrological triggers should also be completed given the high seismicity, rainfall and snow melt levels that affect the site.

### Acknowledgments

Field work was kindly supported by Jana Eichel, Pat Kailey, Tim Stahl, Michal Brezny, James Fay and Florian Strohmaier with laboratory analysis by Georg Stockinger, Fritz Ettl and Till Mayer.

### Funding information

The research was funded by Massey University Research Grant (MR19350), Brian Mason Trust (2017/24) and Deutsche Forschungsgemeinschaft (DR 1070/1-1). The authors acknowledge support by the Department of Conservation. S. Cook and D. Draebing thank Massey University for funding in the form of the Massey University Visiting International Research Fund (2017 and 2018 respectively).

### References

Agliardi F, Crosta G, Zanchi A (2001) Structural constraints on deep-seated slope deformation kinematics. *Eng Geol* 59(1-2):83–102  
 Agliardi F, Crosta GB, Zanchi A, Ravazzi C (2009a) Onset and timing of deep-seated gravitational slope deformations in the eastern Alps, Italy. *Geomorphology* 103(1):113–129

Agliardi F, Zanchi A, Crosta GB (2009b) Tectonic vs. gravitational morphostructures in the central Eastern Alps (Italy): constraints on the recent evolution of the mountain range. *Tectonophysics* 474(1-2):250–270  
 Ambrosi C, Crosta GB (2011) Valley shape influence on deformation mechanisms of rock slopes. *Geol Soc Lond, Spec Publ* 351(1):215–233  
 Archibald, G.C., Carey J.M., Ries. W.F., McColl. S.T., 2016. Geological inspection and baseline monitoring of Mueller Hut, Aoraki/Mt Cook National Park. GNS Science Consultancy Report 2016/80 June 2016  
 Aringoli, D., Farabollini, P., Giacometti, M., Materazzi, M., Paggi, S., Pambianchi, G., Pierantoni, P.P., Pistolesi, E., Pitts, A. and Tondi, E., 2016. The August 24th 2016 Accumoli earthquake: surface faulting and deep-seated gravitational slope deformation (DSGSD) in the Monte Vettore area. *Annals of Geophysics*, 59  
 Ballantyne CK (2002) Paraglacial geomorphology. *Quat Sci Rev* 21(18-19):1935–2017  
 Ballantyne CK, Stone JO (2009) Rock-slope failure at Baosbheinn, Wester Ross, NW Scotland: age and interpretation. *Scott J Geol* 45(2):177–181  
 Ballantyne CK, Stone JO (2013) Timing and periodicity of paraglacial rock-slope failures in the Scottish Highlands. *Geomorphology* 186:150–161  
 Ballantyne CK, Sandeman GF, Stone JO, Wilson P (2014a) Rock-slope failure following Late Pleistocene deglaciation on tectonically stable mountainous terrain. *Quat Sci Rev* 86:144–157  
 Ballantyne CK, Wilson P, Gheorghiu D, Rodés À (2014b) Enhanced rock-slope failure following ice-sheet deglaciation: timing and causes. *Earth Surf Process Landf* 39(7):900–913  
 Barbarano M, Agliardi F, Crosta GB, Zanchi A (2015) Inherited and active tectonic controls on the Piz Dora DSGSD (Val Müstair, Switzerland). In: *Engineering geology for society and territory-volume 2*. Springer, Cham, pp 605–608  
 Beck AC (1968) Gravity faulting as a mechanism of topographic adjustment. *N Z J Geol Geophys* 11(1):191–199  
 Bekler T, Ekinci YL, Demirci A, Erginal AE, Ertekin C (2011) Characterization of a landslide using seismic refraction, electrical resistivity and hydrometer methods, Adatepe–Çanakkale, NW Turkey. *J Environ Eng Geophys* 16(3):115–126  
 Bovis MJ (1982) Uphill-facing (antislope) scarps in the Coast Mountains, southwest British Columbia. *Geol Soc Am Bull* 93(8):804–812  
 Bovis MJ, Evans SG (1996) Extensive deformations of rock slopes in southern Coast Mountains, southwest British Columbia, Canada. *Eng Geol* 44(1-4):63–182  
 Brideau MA, Stead D (2012) Evaluating kinematic controls on planar translational slope failure mechanisms using three-dimensional distinct element modelling. *Geotech Geol Eng* 30(4):991–1011  
 Brideau MA, Yan M, Stead D (2009) The role of tectonic damage and brittle rock fracture in the development of large rock slope failures. *Geomorphology* 103(1):30–49  
 Chigira M, Kiho K (1994) Deep-seated rockslide-avalanches preceded by mass rock creep of sedimentary rocks in the Akaishi Mountains, central Japan. *Eng Geol* 38(3-4):221–230  
 Clarke BA, Burbank DW (2011) Quantifying bedrock-fracture patterns within the shallow subsurface: implications for rock mass strength, bedrock landslides, and erodibility. *J Geophys Res Earth Surf* 116(F4)  
 Clayton A, Stead D, Kinakin D, Wolter A (2017) Engineering geomorphological interpretation of the Mitchell Creek Landslide, British Columbia, Canada. *Landslides* 14(5):1655–1675  
 Cook GK. 2001. Rock mass structure and intact rock strength of New Zealand greywackes. M.Sc. thesis, University of Canterbury  
 Coquin J, Mercier D, Bourgeois O, Cossart E, Decaulne A (2015) Gravitational spreading of mountain ridges coeval with Late Weichselian deglaciation: impact on glacial landscapes in Tröllaskagi, northern Iceland. *Quat Sci Rev* 107:197–213  
 Cossart E, Braucher R, Fort M, Bourlès DL, Carcaillet J (2008) Slope instability in relation to glacial debulking in alpine areas (Upper Durance catchment, southeastern France): evidence from field data and  $^{10}\text{Be}$  cosmic ray exposure ages. *Geomorphology* 95(1-2):3–26  
 Cox SC, Barrell DJA (2007) Geology of the Aoraki area. Institute of Geological and Nuclear Sciences 1:250000 Geological map. GNS Science, Lower Hutt  
 Crosta GB, Agliardi F (2003) Failure forecast for large rock slides by surface displacement measurements. *Can Geotech J* 40(1):176–191  
 Crosta GB, Frattini P, Agliardi F (2013) Deep seated gravitational slope deformations in the European Alps. *Tectonophysics* 605:13–33  
 Crosta GB, Di Prisco C, Frattini P, Frigerio G, Castellanza R, Agliardi F (2014) Chasing a complete understanding of the triggering mechanisms of a large rapidly evolving rockslide. *Landslides* 11(5):747–764  
 Crozier MJ, Deimel MS, Simon JS (1995) Investigation of earthquake triggering for deep-seated landslides, Taranaki, New Zealand. *Quat Int* 25:65–73

- Davis JL, Annan AP (1989) Ground-penetrating radar for high-resolution mapping of soil and rock stratigraphy 1. *Geophysical prospecting* 37(5):531–551
- De Giorgi L, Leucci G (2014) Detection of hazardous cavities below a road using combined geophysical methods. *Surv Geophys* 35(4):1003–1021
- Draebing D, Krautblatter M (2012) P-wave velocity changes in freezing hard low-porosity rocks: a laboratory-based time-average model. *Cryosphere* 6:1163–1174
- Dramis F, Sorriso-Valvo M (1994) Deep-seated gravitational slope deformations, related landslides and tectonics. *Eng Geol* 38(3–4):231–243
- Eberhardt E, Stead D, Coggan JS (2004) Numerical analysis of initiation and progressive failure in natural rock slopes—the 1991 Randa rockslide. *Int J Rock Mech Min Sci* 41(1):69–87
- El Bedoui S, Guglielmi Y, Lebourg T, Pérez JL (2009) Deep-seated failure propagation in a fractured rock slope over 10,000 years: the La Clapière slope, the south-eastern French Alps. *Geomorphology* 105(3–4):232–238
- Fey C, Wichmann V, Zangerl C (2017) Reconstructing the evolution of a deep seated rockslide (Marzell) and its response to glacial retreat based on historic and remote sensing data. *Geomorphology* 298:72–85
- Ganerød GV, Grøneng G, Rønning JS, Dalsegg E, Elvebakk H, Tønnesen JF, Kveldevisk V, Eiken T, Blikra LH, Braathen A (2008) Geological model of the Åknes rockslide, western Norway. *Eng Geol* 102(1):1–18
- Geertsema M, Clague JJ, Schwab JW, Evans SG (2006) An overview of recent large catastrophic landslides in northern British Columbia, Canada. *Eng Geol* 83(1–3):120–143
- Gellatly AF (1985) Historical records of glacier fluctuations in Mt Cook National Park, New Zealand: a century of change. *Geogr J* 151(1):86–99
- Ghirotti, M., Martin, S. and Genevois, R., 2011. The Celentino deep-seated gravitational slope deformation (DSGSD): structural and geomechanical analyses (Peio Valley, NE Italy). Geological Society, London, Special Publications, 351(1), 235–251
- Glastonbury J, Fell R (2008a) Geotechnical characteristics of large slow, very slow, and extremely slow landslides. *Can Geotech J* 45(7):984–1005
- Glastonbury J, Fell R (2008b) A decision analysis framework for the assessment of likely post-failure velocity of translational and compound natural rock slope landslides. *Can Geotech J* 45(3):329–350
- Glastonbury J, Fell R (2010) Geotechnical characteristics of large rapid rock slides. *Can Geotech J* 47(1):116–132
- Glueer F, Loew S, Manconi A (2019) Paraglacial history and structure of the Moosfluh Landslide. *Geomorphology*.
- Gori S, Falucchi E, Dramis F, Galadini F, Galli P, Giaccio B, Messina P, Pizzi A, Sposato A, Cosentino D (2014) Deep-seated gravitational slope deformation, large-scale rock failure, and active normal faulting along Mt. Morrone (Sulmona basin, Central Italy): geomorphological and paleoseismological analyses. *Geomorphology* 208:88–101
- Grämiger LM, Moore JR, Gischig VS, Ivy-Ochs S, Loew S (2017) Beyond debuttreasing: mechanics of paraglacial rock slope damage during repeat glacial cycles. *J Geophys Res Earth Surf* 122(4):1004–1036
- Grämiger LM, Moore JR, Gischig VS, Loew S (2018) Thermomechanical stresses drive damage of Alpine valley rock walls during repeat glacial cycles. *J Geophys Res Earth Surf* 123(10):2620–2646
- Hancox, G. T., 1994. Report on Mt Cook National Park hut site inspections and establishment of monitoring lines, April 1994. Institute of Geological and Nuclear Sciences, Client Report 353902.20, prepared for Department of Conservation, Mt. Cook National Park; 32
- Hancox, G.T., 1998. Pilot study for Baseline Geological Inspection of DOC Backcountry Huts: inspections of alpine hut sites in the Mt Cook and Westland National Parks, March 1998. Institute of Geological and Nuclear Sciences Client Report 43713B
- Hauck C, Vonder Mühl D (2003) Evaluation of geophysical techniques for application in mountain permafrost studies. *Z Geomorphol Suppl* 132:161–190
- Havenith HB, Jongmans D, Abdrakmatov K, Trefois P, Delvaux D, Torgoev IA (2000) Geophysical Investigations of seismically induced surface effects: case study of a landslide in the Suusamyr Valley, Kyrgyzstan. *Surv Geophys* 21(4):351–370
- Havenith HB, Jongmans D, Faccioli E, Abdrakmatov K, Bard PY (2002) Site effect analysis around the seismically induced Ananevo Rockslide, Kyrgyzstan. *Bull Seismol Soc Am* 92(8):3190–3209
- Heincke B, Maurer H, Green AG, Willenberg H, Spillmann T, Burlini L (2006) Characterizing an unstable mountain slope using shallow 2D and 3D seismic tomography. *Geophysics* 71(6):241–256
- Heincke B, Günther T, Dalsegg E, Rønning JS, Ganerød GV, Elvebakk H (2010) Combined three-dimensional electric and seismic tomography study on the Åknes rockslide in western Norway. *J Appl Geophys* 70(4):292–306
- Hewitt K, Clague JJ, Orwin JF (2008) Legacies of catastrophic rock slope failures in mountain landscapes. *Earth Sci Rev* 87(1–2):1–38
- Hou Y, Chigira M, Tsou CY (2014) Numerical study on deep-seated gravitational slope deformation in a shale-dominated dip slope due to river incision. *Eng Geol* 179:59–75
- Hungr O (2007) Dynamics of rapid landslides. In: *Progress in landslide science*. Springer, Berlin, pp 47–57
- Hungr O, Leroueil S, Picarelli L (2014) The Varnes classification of landslide types, an update. *Landslides* 11(2):167–194
- Jaboyedoff M, Penna I, Pedrazzini A, Baroň I, Crosta GB (2013) An introductory review on gravitational-deformation induced structures, fabrics and modeling. *Tectonophysics* 605:1–12
- James MR, Robson S (2014) Mitigating systematic error in topographic models derived from UAV and ground-based image networks. *Earth Surf Process Landf* 39(10):1413–1420
- Kilburn CR, Petley DN (2003) Forecasting giant, catastrophic slope collapse: lessons from Vajont, Northern Italy. *Geomorphology* 54(1–2):21–32
- Kirkbride MP, Warren CR (1999) Tasman Glacier, New Zealand: 20th-century thinning and predicted calving retreat. *Glob Planet Chang* 22(1–4):11–28
- Kliche CA (1999) Rock slope stability. SME, Littleton
- Kos A, Amann F, Strozzi T, Delaloye R, Ruette J, Springman S (2016) Contemporary glacier retreat triggers a rapid landslide response, Great Aletsch Glacier, Switzerland. *Geophys Res Lett* 43(24):466–474
- Krautblatter M, Draebing D (2014) Pseudo 3D - P-wave refraction seismic monitoring of permafrost in steep unstable bedrock. *J Geophys Res Earth Surf* 119(2):287–299
- Lillie AR, Gunn BM (1964) Steeply plunging folds in the Sealy Range, southern Alps. *N Z J Geol Geophys* 7(3):403–423
- Mahr T (1977) Deep—Reaching gravitational deformations of high mountain slopes. *IAEST* 16(1):121–127
- Marinos V, Marinos P, Hoek E (2005) The geological strength index: applications and limitations. *Bull Eng Geol Environ* 64(1):55–65
- Martinotti, G., Giordan, D., Giardino, M. and Ratto, S., 2011. Controlling factors for deep-seated gravitational slope deformation (DSGSD) in the Aosta Valley (NW Alps, Italy). Geological Society, London, Special Publications, 351(1), 113–131
- Matsui T, San K-C (1992) Finite element slope stability analysis by shear strength reduction technique. *Soils Found* 32:59–70
- McColl ST (2012a) Paraglacial rock-slope stability. *Geomorphology* 153:1–16
- McColl, S.T., 2012b. Paraglacial Rockslope Stability. Phd Thesis, University of Canterbury
- McColl ST, Davies THR (2013) Large ice-contact slope movements: glacial buttressing, deformation and erosion. *Earth Surf Process Landf* 38(10):1102–1115
- McColl ST, Draebing D (2019) Rock slope instability in the proglacial zone: State of the Art. In: Heckmann T, Morche D (eds) *Geomorphology of proglacial systems - landform and sediment dynamics in recently deglaciated alpine landscapes*, pp 119–141
- Meric O, Garambois S, Jongmans D, Wathélet M, Chatelain JL, Vengeon JM (2005) Application of geophysical methods for the investigation of the large gravitational mass movement of Séchillienne, France. *Can Geotech J* 42(4):1105–1115
- Nemcok A, Pasek J, Rybar J (1972) Classification of landslides and other mass movements. *Rock Mechanics Felsmechanik Mecanique des Roches* 4:71–78
- Nishii R, Matsuoka N, Daimaru H, Yasuda M (2013) Precursors and triggers of an alpine rockslide in Japan: the 2004 partial collapse during a snow-melting period. *Landslides* 10(1):75–82
- Oppikofer T, Jaboyedoff M, Pedrazzini A, Derron MH, Blikra LH (2011) Detailed DEM analysis of a rockslide scar to characterize the basal sliding surface of active rockslides. *J Geophys Res Earth Surf* 116(F2)
- Pánek T, Klimeš J (2016) Temporal behavior of deep-seated gravitational slope deformations: a review. *Earth Sci Rev* 156:14–38
- Pánek T, Hradecký J, Minár J, Hungr O, Dušek R (2009) Late Holocene catastrophic slope collapse affected by deep-seated gravitational deformation in flysch: Ropice Mountain, Czech Republic. *Geomorphology* 103(3):414–429
- Pánek T, Brázdil R, Klimeš J, Smolková V, Hradecký J, Zahradníček P (2011a) Rainfall-induced landslide event of May 2010 in the eastern part of the Czech Republic. *Landslides* 8(4):507–516
- Pánek T, Tábořík P, Klimeš J, Komárková V, Hradecký J, Štátný M (2011b) Deep-seated gravitational slope deformations in the highest parts of the Czech Flysch Carpathians: evolutionary model based on kinematic analysis, electrical imaging and trenching. *Geomorphology* 129(1–2):92–112
- Pánek T, Šilhán K, Tábořík P, Hradecký J, Smolková V, Lenart J, Brázdil R, Kašičková L, Pazdura A (2011c) Catastrophic slope failure and its origins: Case of the May 2010 Girová Mountain long-runout rockslide (Czech Republic). *Geomorphology* 130(3–4):352–364
- Phillips M, Haberkorn A, Draebing D, Krautblatter M, Rhyner H, Kenner R (2016) Seasonally intermittent water flow through deep fractures in an Alpine rock ridge: Gemsstock, central Swiss Alps. *Cold Reg Sci Technol* 125:117–127

- Price NJ, Cosgrove JW (1990) Analysis of geological structures. Cambridge University Press
- Radbruch-Hall DH (1978) Gravitational creep of rock masses on slopes. In *Developments in Geotechnical Engineering* 14:607–657
- Ridl R, Bell D, Villeneuve M (2017) Application of finite element method of numerical modelling to understand toe buckling deformation in the Southern Alps of New Zealand. In: *EGU General Assembly Conference Abstracts*, vol 19, p 13689
- Riva F, Agliardi F, Amitrano D, Crosta GB (2018) Damage-based time-dependent modeling of paraglacial to postglacial progressive failure of large rock slopes. *J Geophys Res Earth Surf* 123(1):124–141
- Rocscience (2017) RocData version 5.009. Rocscience Inc, Toronto
- Rocscience 2019. RS2 2D Geotechnical finite element analysis, version 2019 10.008. Rocscience Inc. Toronto
- Sandmeier KJ (2012) REFLEXW Version 7.0 Manual, Karlsruhe
- Sturzenegger M, Stead D (2012) The Palliser Rockslide, Canadian Rocky Mountains: characterization and modeling of a stepped failure surface. *Geomorphology* 138(1):145–161
- Tannant DD, Giordan D, Morgenroth J (2017) Characterization and analysis of a translational rockslide on a stepped-planar slip surface. *Eng Geol* 220:144–151
- Theune U, Rokosh D, Sacchi MD, Schmitt DR (2006) Mapping fractures with GPR: A case study from Turtle Mountain. *Geophysics* 71(5):B139–B150
- Toshioka T, Tsuchida T, Sasahara K (1995) Application of GPR to detecting and mapping cracks in rock slopes. *Journal of Applied Geophysics* 33(1–3):119–124
- Winkler S (2018) Investigating Holocene mountain glaciations: a plea for the supremacy of glacial geomorphology when reconstructing glacier chronologies. *Erdkunde* 72:215–234
- E. Cody** (✉) · **S. McColl**  
Geosciences Group, School of Agriculture and Environment,  
Massey University,  
Palmerston North, New Zealand  
Email: emma.cody@hotmail.co.nz
- D. Draebing**  
University of Bayreuth,  
Bayreuth, Germany
- D. Draebing**  
Technical University of Munich,  
Munich, Germany
- S. Cook**  
Geography and Environmental Science, School of Social Sciences,  
University of Dundee,  
Dundee, UK
- M.-A. Brideau**  
GNS Science,  
Lower Hutt, New Zealand